

Report PME-FM-90-2

AD-A217 308

THE EFFECT OF ADVERSE PRESSURE GRADIENT ON TURBULENT BURST STRUCTURE IN LOW-REYNOLDS NUMBER EQUILIBRIUM BOUNDARY LAYERS

Jack B. White and William G. Tiederman  
School of Mechanical Engineering  
Purdue University  
West Lafayette, Indiana 47907

January, 1990

Technical Report for Period 01 December 1988 - 30 November 1989

DTIC  
ELECTE  
JAN 30 1990  
S E D

Approved for public release, distribution unlimited

Prepared for

OFFICE OF NAVAL RESEARCH  
800 North Quincy Street  
Arlington, VA 22217-5000

REPORT DOCUMENTATION PAGE		READ INSTRUCTIONS BEFORE COMPLETING FORM
1. REPORT NUMBER PME-FM-90-2	2. GOVT ACCESSION NO.	3. RECIPIENT'S CATALOG NUMBER
4. TITLE (and Subtitle) THE EFFECT OF ADVERSE PRESSURE GRADIENT ON THE TURBULENT BURST STRUCTURE IN LOW- REYNOLDS NUMBER EQUILIBRIUM BOUNDARY LAYERS		4. TYPE OF REPORT & PERIOD COVERED Technical Report for 01 December 1988 through 30 November, 1989
		6. PERFORMING ORG. REPORT NUMBER
7. AUTHOR(s)  Jack B. White, William G. Tiederman		8. CONTRACT OR GRANT NUMBER(s)  N00014-83K-0183
9. PERFORMING ORGANIZATION NAME AND ADDRESS School of Mechanical Engineering Purdue University West Lafayette, Indiana 47907		10. PROGRAM ELEMENT, PROJECT, TASK AREA & WORK UNIT NUMBERS  4322-754
11. CONTROLLING OFFICE NAME AND ADDRESS Office of Naval Research 800 North Quincy Street Arlington, VA 22217-5000		12. REPORT DATE January, 1990
		13. NUMBER OF PAGES 72
14. MONITORING AGENCY NAME & ADDRESS (if different from Controlling Office)		15. SECURITY CLASS. (of this report)
		15a. DECLASSIFICATION/DOWNGRADING SCHEDULE
16. DISTRIBUTION STATEMENT (of this Report)  <p style="text-align: center;">APPROVED FOR PUBLIC RELEASE: DISTRIBUTION UNLIMITED</p>		
17. DISTRIBUTION STATEMENT (of the abstract entered in Block 20, if different from Report)		
18. SUPPLEMENTARY NOTES		
19. KEY WORDS (Continue on reverse side if necessary and identify by block number)  Turbulent boundary layers, Adverse pressure gradients, equilibrium boundary layers.		
20. ABSTRACT (Continue on reverse side if necessary and identify by block number)  This study is an investigation of low Reynolds number, zero and adverse pressure gradient, equilibrium boundary layers. Two adverse pressure gradient boundary layers and one zero pressure gradient boundary layer were studied with the zero pressure		

gradient case serving as a comparative standard for the non-zero pressure gradient boundary layers. The non-zero cases included a mild pressure gradient and a strong (relative to the mild case) pressure gradient. The objective of the study was to determine the effect of pressure gradient on the turbulent burst structure for these flows. The Reynolds number (based on momentum thickness),  $R_{\theta}$ , varied from 1120 to 2500 and the pressure gradient parameter,  $\beta$ , varied from 0.0 to 1.8. Single component laser Doppler velocimeter measurements were made of the streamwise velocity to determine the various boundary layer integral parameters and to create velocity records needed to calculate the period of the bursting cycle.

Over the range of Reynolds numbers studied, the results indicate that the burst period (normalized with inner variables) is not a function of Reynolds number. The burst period appears to be solely a function of the pressure gradient and upstream history of the boundary layer. Although the period of the burst cycle is reduced by the adverse pressure gradient, the ensemble averaged velocity signature of the bursts do not change. This indicates that the nature of the individual burst is not significantly changed by the presence of the adverse pressure gradient.

# TABLE OF CONTENTS

	Page
LIST OF FIGURES.....	iv
LIST OF TABLES .....	vi
LIST OF SYMBOLS.....	vii
CHAPTER ONE - INTRODUCTION.....	1
CHAPTER TWO - APPARATUS AND PROCEDURE .....	6
2.1 Boundary Layer Facility.....	6
2.2 Laser Doppler Velocity Measurements .....	9
2.3 Procedure for Setting Flow Conditions.....	12
CHAPTER THREE - RESULTS.....	16
3.1 Evaluation of Shear Velocity .....	16
3.2 Zero Pressure Gradient Flow .....	21
3.3 Mild Adverse Pressure Gradient Flow .....	26
3.4 Strong Adverse Pressure Gradient.....	28
3.5 Variation of the von Karman Constant and Intercept.....	32
3.6 Turbulent Burst Structure.....	34
CHAPTER FOUR - CONCLUSIONS .....	48
REFERENCES .....	50
Appendix A Two-dimensionality Verification.....	52
Appendix B Uncertainty Analysis .....	55
Appendix C Wall Shapes.....	57
Appendix D Tabulated Velocity Data .....	59



<b>Accession For</b>	
NTIS GRA&I	<input checked="" type="checkbox"/>
DTIC TAB	<input type="checkbox"/>
Unannounced	<input type="checkbox"/>
Justification	
By _____	
Distribution/	
Availability Codes	
Dist	Avail and/or Special
A-1	

## LIST OF FIGURES

Figure	Page
2.1. Schematic of flow loop. . . . .	7
2.2. Schematic of laser Doppler velocimetry optics. . . . .	11
3.1. Calculated shear velocity for zero pressure gradient flow, $R_\theta = 1530$ ; $\square$ , $u_{\tau_{\text{calculated}}}$ ; — — — —, $u_\tau$ mean. . . . .	17
3.2. Linear velocity profile in the viscous sublayer. . . . .	19
3.3. Mean velocity profiles for zero pressure gradient flow. . . . .	22
3.4. Comparison of mean velocity profile at $R_\theta = 1410$ . . . . .	22
3.5. Velocity defect profiles for zero pressure gradient boundary layer. . . . .	24
3.6. RMS of streamwise velocity for zero pressure gradient flow. . . . .	24
3.7. RMS of streamwise velocity for zero pressure gradient at $R_\theta = 1410$ . . . . .	25
3.8. Mean velocity profiles for mild pressure gradient boundary layer. . . . .	27
3.9. Velocity defect profiles for mild pressure gradient boundary layer. . . . .	27
3.10. RMS of streamwise velocity for mild pressure gradient flow. . . . .	29
3.11. Mean velocity profiles for strong adverse pressure gradient flow. . . . .	29
3.12. Velocity defect profiles for strong adverse pressure gradient flow. . . . .	31
3.13. RMS of streamwise velocity for strong adverse pressure gradient flow. . . . .	31
3.14. Probability plot for time between ejections. Zero pressure gradient flow, $R_\theta = 1540$ , $L = 0.60$ . . . . .	35
3.15. Period of the burst cycle, $\bar{T}_b$ , as a function of threshold, $L$ , for zero pressure gradient flow at $R_\theta = 1540$ . . . . .	37
3.16. Burst period, $\bar{T}_b^+$ , as a function of Reynolds number for all flows. . . . .	39
3.17. Normalized burst period, $\bar{T}_b^+$ , as a function of the equilibrium parameter, $\beta$ . . . . .	40

Figure	Page
3.18. Normalized burst period, $\bar{T}_b^+$ , as a function of the Clauser shape factor, G. . . . .	42
3.19. Normalized burst period, $\bar{T}_b^+$ , as a function of the pressure gradient parameter, K. . . . .	43
3.20. Conditionally averaged streamwise velocity signals centered on the burst leading edge. . . . .	45
3.21. Conditionally averaged streamwise velocity signals centered on the burst trailing edge. . . . .	46
 Appendix	
Figure	
A.1 Two-dimensionality verification for zero pressure gradient at station one. . . . .	52
A.2 Two-dimensionality verification for zero pressure gradient at station four. . . . .	52
A.3 Two-dimensionality verification for mild adverse pressure gradient at station one. . . . .	53
A.4 Two-dimensionality verification for mild adverse pressure gradient at station four. . . . .	53
A.5 Two-dimensionality verification for strong adverse pressure gradient at station one. . . . .	54
A.6 Two-dimensionality verification for strong adverse pressure gradient at station four. . . . .	54

## LIST OF TABLES

Table	Page
1.1. Flow parameters. . . . .	4
3.1. Shear velocity (mm/sec) using three methods. . . . .	20
3.2 Von Karman constant and intercept . . . . .	33
3.3 Number of ejections per burst. . . . .	47
Appendix	
Table	
C.1 Wall shape for zero pressure gradient case . . . . .	57
C.2 Wall shape for mild adverse pressure gradient case . . . . .	57
C.3 Wall shape for strong adverse pressure gradient case . . . . .	58
D.1 Zero pressure gradient - station 1 . . . . .	59
D.2 Zero pressure gradient - station 2 . . . . .	60
D.3 Zero pressure gradient - station 3 . . . . .	61
D.4 Zero pressure gradient - station 4 . . . . .	62
D.5 Mild adverse pressure gradient - station 1 . . . . .	63
D.6 Mild adverse pressure gradient - station 2 . . . . .	64
D.7 Mild adverse pressure gradient - station 3 . . . . .	65
D.8 Mild adverse pressure gradient - station 4 . . . . .	66
D.9 Strong adverse pressure gradient - station 1 . . . . .	67
D.10 Strong adverse pressure gradient - station 2 . . . . .	68
D.11 Strong adverse pressure gradient - station 3 . . . . .	69
D.12 Strong adverse pressure gradient - station 4 . . . . .	70

## LIST OF SYMBOLS

Symbol	Description
B	intercept of the law of the wall
G	Clauser (1954) shape factor, $G = H(U_e/u_\tau)$
H	shape factor, $H = \delta^*/\theta$
K	pressure gradient parameter, $K = (v/U_e^2)dU_e/dx$
L	threshold for modified u-level ejection detection technique
RMS	root mean square
$R_\theta$	Reynolds number based on the momentum thickness, $\theta$
$\bar{T}_b$	average period of the bursting cycle
U	instantaneous velocity in the streamwise direction
$U_e$	freestream velocity
$u'$	RMS of streamwise velocity
$u_\tau$	shear velocity
x	streamwise direction
y	normal direction
$\beta$	equilibrium parameter, $\beta = (\delta^*/\tau_w)dP/dx$
$\Delta$	Clauser (1954) thickness, $\Delta = \delta^*U_e/u_\tau$
$\delta^*$	displacement thickness
$\kappa$	von Karman constant in the law of the wall
$\nu$	kinematic viscosity
$\tau_w$	wall shear stress

Symbol	Description
$\theta$	momentum thickness
Superscripts	
+	normalized with inner variables, $u_\tau$ and $v$
-	time average
'	root mean square (RMS)

## CHAPTER ONE - INTRODUCTION

The nature of turbulent boundary layer flow is still far from completely understood. In many years of investigation, much has been done in studying and understanding the structure of zero pressure gradient turbulent boundary layers. Much less attention has been devoted to the study of non-zero pressure gradient boundary layers. Kline (1988) reviewed the current status of the structural understanding of turbulent boundary layers. He identifies eight categories of quasi-coherent structures in the flat-plate, zero pressure gradient turbulent boundary layer. Most real-world fluid devices impose a pressure gradient on the fluid that passes over or through them. Aircraft, diffusers and compressors are just a few of the devices which are limited by the ability of the boundary layer to react to the imposed pressure gradient. The design of fluid devices can only benefit from a further understanding of how pressure gradient affects the coherent structures. Kline (1988) identifies the ejection of low-speed fluid outward from the wall as an important structure which plays a major role in the production of turbulence and in momentum transport. For this reason, this study undertakes to determine the effect of pressure gradient on this very important aspect of the turbulent structure of turbulent boundary layers.

Kim *et al.* (1971) and Corino and Brodkey (1969) showed that most of the turbulence production and momentum transport occur during the events known as "bursts and sweeps". Coherent filaments of slow speed fluid in the very near wall region ( $y^+ \leq 5$ ), called streaks, move slowly downstream. The (+) superscript denotes normalization with the kinematic viscosity,  $\nu$ , and the shear velocity,  $u_\tau = \sqrt{\tau_w/\rho}$ . These streaks eventually begin to move away from the wall until at  $y^+ \approx 15$  they oscillate and eject violently away

from the wall. One or more ejections of slow speed fluid from the same streak is called a "burst". The sweep event is a rush of high-speed fluid from the outer flow towards the wall which interacts with the slower moving fluid in the wall region. Because the burst event is a major player in the production of turbulence and momentum transport, a proper understanding of this event is important to providing accurate turbulence models. The burst event is thought to occur in a quasi-periodic manner. Thus, an important statistical quantity associated with the burst event is the average period of the bursting cycle. This study will attempt to determine the effect of adverse pressure gradient and Reynolds number on the average period of the bursting cycle, the conditionally averaged burst velocity signature, and the number of ejections occurring per burst.

An earlier study described by Kline *et al.* (1967) used flow visualization to determine the streak and burst structure. The information obtained indicated that the presence of an adverse pressure gradient serves to decrease the average burst period. The study described by Kline only gives qualitative information on the burst period because the technique used to count the bursts was done over a certain streamwise extent of the wall and the author noted that the number of bursts visualized changed as a function of the distance downstream from the dye injection. The method currently accepted for counting the burst rate is to count only those bursts passing through a single point. Streak spacing is not measured in the present study, but Kline *et al.* (1967) showed that the streak spacing normalized with inner variables is a constant over the range of pressure gradients investigated in the present study.

Using simultaneous flow visualization and velocity measurements, Luchik and Tiederman (1987) showed that several techniques could be used to deduce the average burst period from single point velocity measurements. Two successful burst detection methods are the uv-quadrant two technique and the modified u-level technique. Both of these techniques detect the ejection of slow speed fluid from the streak. Several of these

ejections of fluid can occur from a single streak as shown by Bogard and Tiederman (1986). A distinction must be made between the "ejection" event and the "burst" event. A burst can be made up of several ejections from the same streak. These detection methods are actually ejection detection methods and determine the number of ejections occurring, but, by themselves, do not distinguish between ejections from the same burst and ejections from different bursts. The uv-quadrant two technique requires simultaneous measurement of both the streamwise and wall normal components of velocity. This technique detects the large negative uv spike along with the positive spike in the wall-normal velocity,  $v$ , associated with an ejection. The modified u-level technique takes advantage of the large decrease in streamwise velocity which occurs when an ejection passes through the measuring volume. This technique requires only measurement of the streamwise component of velocity. The modified u-level technique was chosen for the present study, thus allowing the less complicated task of performing only single component velocity measurements in the streamwise direction.

Clauser (1954) argued that the structure of turbulent boundary layers was not merely a function of the local conditions, but also depended on a long portion of upstream history. White (1974) noted that at least five boundary layer thicknesses were necessary for a boundary layer to come to "equilibrium" after being introduced to an abrupt change in pressure gradient such as that found when a pressure gradient is suddenly removed. For this reason, it is believed that the turbulent burst structure will be a function of not only the local Reynolds number and pressure gradient, but also of the previous pressure gradient history in the layer. In order to quantify the upstream history of the boundary layers, equilibrium boundary layers as defined by Clauser (1954) were chosen for this study. An equilibrium boundary layer is defined as one in which the equilibrium parameter,  $\beta$ , where

$$\beta = \frac{\delta^*}{\tau_w} \frac{dP}{dx} \quad (1.1)$$

remains constant throughout the streamwise extent of the boundary layer. Note that  $\tau_w$  is the wall shear stress and  $\delta^*$  is the boundary layer displacement thickness. This is a useful parameter for studying the effect of pressure gradient on the turbulent structure of an equilibrium boundary layer because it characterizes both the pressure gradient and the upstream history of the boundary layer.

Table 1.1 shows the experimental locations at which profiles of the streamwise velocity and velocity records for measuring the burst period were performed. Measurements were performed at each of four measuring locations for one zero pressure gradient and two adverse pressure gradient boundary layer flows.

Table 1.1 - Flow parameters

$\beta$	$x$ (cm)	$Re_\theta$	$U_e$ (m/sec)	$u_\tau$ (mm/sec)	$\delta^*$ (cm)
0.0	38.5	1120	0.260	12.0	0.57
0.0	65.6	1260	0.260	11.8	0.64
0.0	90.1	1410	0.260	11.7	0.71
0.0	124.5	1540	0.259	11.4	0.77
0.8	38.0	1265	0.246	10.4	0.72
0.8	66.5	1530	0.234	9.4	0.92
0.7	90.0	1780	0.229	9.1	1.08
0.8	125.0	2090	0.220	8.5	1.32
1.7	38.1	1315	0.236	8.8	0.82
1.8	65.5	1796	0.221	8.4	1.22
1.8	90.4	2085	0.210	7.6	1.48
1.7	124.3	2495	0.201	7.0	1.86

The intent of this thesis is to determine the effect of adverse pressure gradient on the turbulent burst structure. This information will provide a data base that can be used to construct new turbulence models that include the important physics of the burst phenomena. Chapter two of this thesis contains information about the apparatus and experimental procedure used in this study. Chapter three contains the results for a zero pressure gradient and two adverse pressure gradient flows. Chapter four contains the conclusions drawn from the study.

## CHAPTER TWO - APPARATUS AND PROCEDURES

### 2.1 Boundary Layer Facility

The experiments were conducted in a variable geometry boundary layer facility. The water flow facility was designed such that the cross sectional area can be varied as a function of the streamwise distance,  $x$ . The flow loop is recirculating and driven by four ninety gallon per minute pumps. A schematic of the flow loop can be seen in figure 2.1.

Large stilling tanks are placed at each end of the test section to damp out any large scale disturbances. The upstream tank has a perforated plate and an open cell sponge section to damp out large scale fluctuations in the flow. The upstream tank is linked to the flow channel via a smooth contraction section. The flow is contracted from the 58 x 58 cm upstream tank to the 41 x 20.5 cm flow channel entrance. Immediately following the contraction is a polycarbonate honey comb section which has a 2.54 cm thickness and a 0.318 cm cell size. This serves to damp any large scale vorticity generated in the contraction. The downstream tank is equipped with a cooling coil to allow the channel water to be maintained at a constant temperature. These experiments were all performed at  $24.5 \pm 0.5$  ° C.

The boundary layer channel is made of two sections. The upstream section merely provides a length over which a laminar boundary layer develops. The flow is enclosed on four sides and hence a boundary layer develops on all four walls. Therefore, the flow is tripped on each wall at the connection between the upstream and downstream sections to avoid separation of the laminar boundary layer as it comes under the influence of the

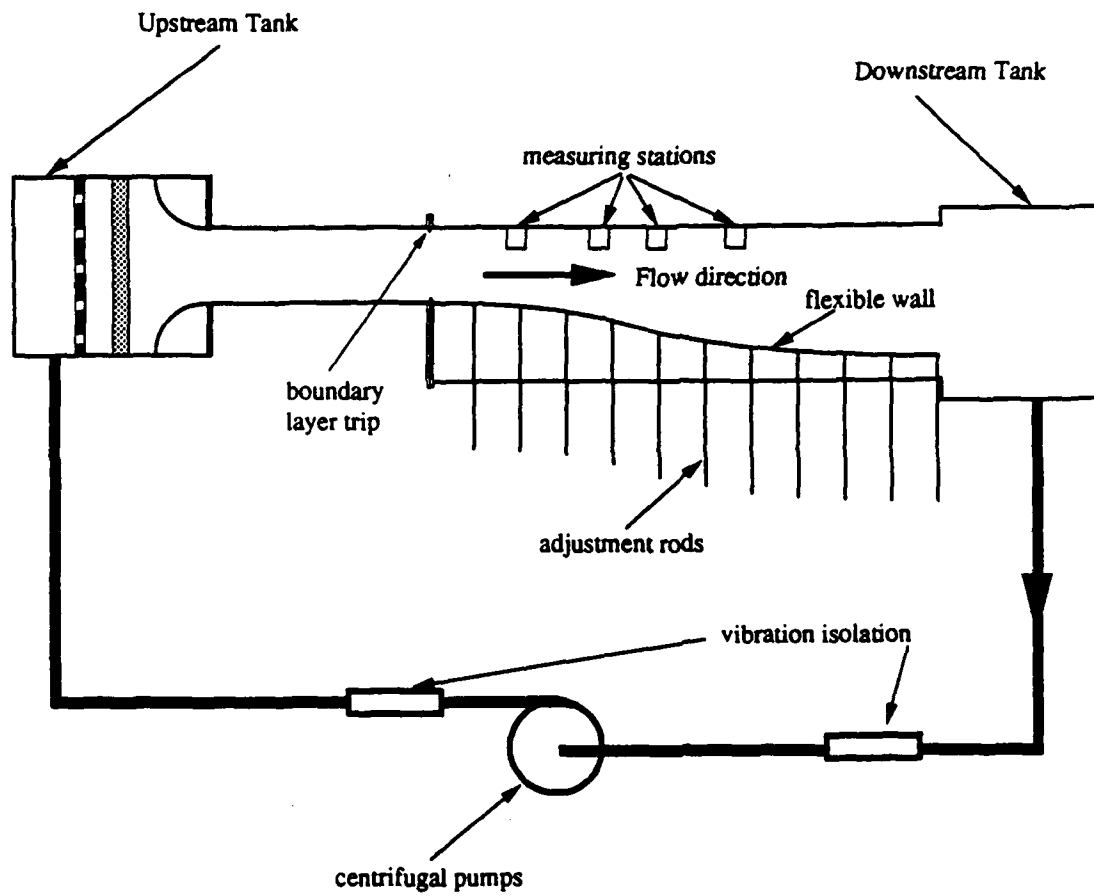


Figure 2.1 Schematic of flow loop.

imposed pressure gradient. The trips are made of 0.318 cm (1/8") brass tubing and are located 100 cm downstream of the inlet. The main test section is in the downstream portion of the facility. The boundary layers investigated were developed on a straight vertical side wall of the channel facility. This wall is a smooth, 244 cm long, 40.6 cm wide, 1.27 cm polycarbonate sheet.

The streamwise pressure gradient is controlled by adjusting the opposing vertical wall which is made of a flexible acrylic sheet. This wall is made of 0.318 cm thick acrylic and has twenty-eight adjustment rods attached to its back side. These adjustment rods allow the wall position to be varied smoothly along the flow direction. Thus the cross sectional area of the channel can be made an arbitrary function of the streamwise distance,  $x$ . The facility was designed such that no more than 40% of the channel width would be within the boundary layer flow, leaving at least 60% of the flow as a potential core flow. Because of this freestream flow in the center of the channel, the pressure gradient along the flat wall is a function of only the freestream velocity as given by Bernoulli's equation:

$$\frac{dP}{dx} = -\rho U_e \frac{dU_e}{dx} \quad (2.1)$$

Where  $P$  is the static pressure,  $\rho$  is the fluid density, and  $U_e$  is the freestream velocity.

The two-dimensionality of the flow was verified by laser Doppler velocity (LDV) measurements of the mean velocity profiles taken at a spanwise location offset 10.2 cm from the center of the channel. These profiles are presented in Appendix A.1. The flow is not two dimensional over the entire width of the measuring wall due to boundary layer growth on the end walls. The two-dimensionality profiles verified that at least 20 cm about the center of the flat vertical plate was two dimensional. The flow was considered two dimensional when profiles at different spanwise locations varied by less than 5%.

By use of the combination of perforated plate, sponge section, and the honeycomb, a freestream turbulence intensity of 0.7% was obtained. Care had to be taken in making the

LDV measurements so that noise in the signal did not yield a higher than actual turbulence intensity. The important factor in doing this was obtaining a sufficiently high signal to noise ratio while keeping the absolute noise level to a minimum. Various methods were tried and in the end a combination of careful shielding of the receiving optics from optical noise, and use of 2  $\mu\text{m}$  polyvinyl seed particles enabled the measurement of the 0.7% turbulence intensity. This was obtained with a signal to noise ratio of approximately 100. When this signal to noise level was reduced to 50 (an acceptable level in highly turbulent flows) a turbulence intensity of 1.2% was measured for the same flow. The counter-type signal processor used in this LDV set-up is not suited for measuring low turbulence intensities. Therefore, the actual turbulence intensity in the channel may have been somewhat less than the measured value.

## 2.2 Laser Doppler Velocity Measurements

Boundary layer velocity measurements were made using a one-component TSI laser Doppler velocimeter system. The streamwise component of velocity,  $U$ , was measured. The system included a TSI model 9180 frequency shifter which allowed shifting of the Doppler frequency to measure possible flow reversals, and to eliminate fringe bias. A TSI model 1980 counter-type LDV signal processor was used to condition and digitize the signal.

A 350 mm focal length lens was used in the transmitting optics to focus the two beams at their crossing to form the volume from which a Doppler signal occurs. A similar lens was used to receive the scattered light from the probe volume. Viewing the probe volume  $7^\circ$  off axis and using a 50  $\mu\text{m}$  aperture in the receiving optics yielded a probe volume with a length of 0.99 mm, a diameter of 50  $\mu\text{m}$ , and a fringe spacing of 3.70  $\mu\text{m}$ . This yields a non-dimensional probe volume length of  $l^+ = 13$  for the zero pressure gradient

case, and  $l^+ = 9$  for the strong adverse pressure gradient case. The channel was designed with windows, made of optical quality glass, in the bottom wall at four different streamwise locations which allowed access to the channel for the transmitted light. Exactly opposite these windows on the top wall were four windows used for receiving the light scattered in the forward direction. Figure 2.2 shows a schematic of this LDV set-up showing the traversing mechanism which allowed the probe volume to be traversed back and forth normal to the wall. Note that the receiving optics are positioned off-axis such that the laser beams do not enter the receiving lens. This is important in reducing the signal to noise to an acceptable level. The receiving optics were also mounted on the traversing mechanism so that they would remain focused on the probe volume as it was moved. The receiving optics could also be adjusted independently in all three dimensions to allow the focus to be "fine tuned" at each traverse location. The flow was seeded with 2.02  $\mu\text{m}$  diameter spheres made of polyvinyltoluene. These provided excellent light scattering, and resulted in signal to noise ratios greater than 50. Care was taken to ensure that on average no more than one particle at a time resided in the probe volume.

The use of the LDV allows measured measurements to be made in the very near wall region. The non-invasive nature of the LDV is ideally suited for such near wall measurements. In order to prevent the possibility of velocity bias, it is necessary to obtain a data rate of at least the viscous frequency,  $u_\tau^2/\nu$ . As the probe volume is positioned closer and closer to the wall, the amount of available scattered light is reduced. Also the optical noise increases due to light reflected off the wall. At some point close to the wall these effects combine to make it impossible to obtain the necessary data rate while maintaining a sufficiently low signal to noise ratio. This sets the limit on how close to the wall measurements can be performed

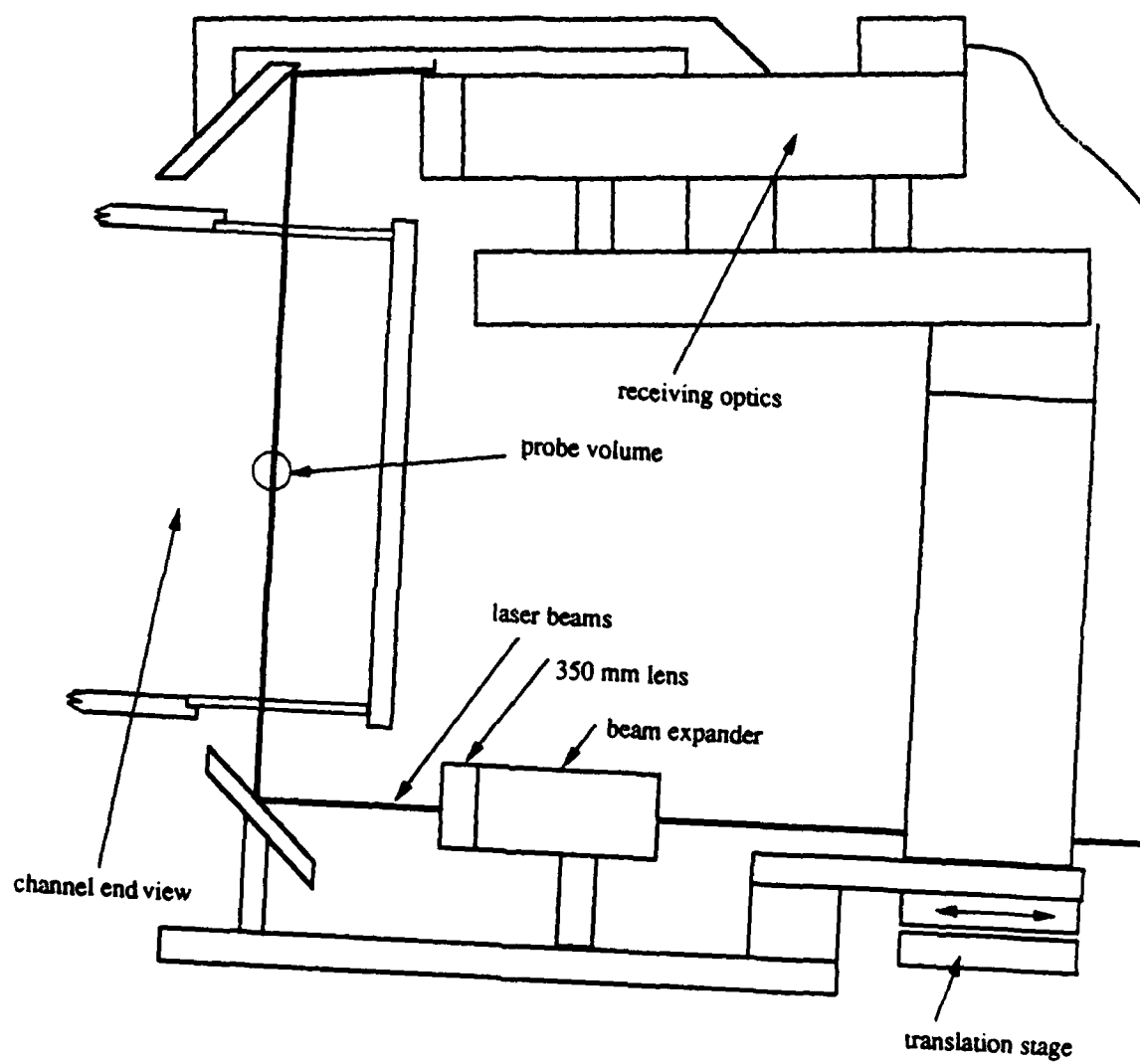


Figure 2.2. Channel end view showing laser Doppler velocimetry optics.

### 2.3 Procedure for Setting Flow Conditions

Since it was necessary to define the upstream history of the boundary layer, it was decided to perform the measurements in equilibrium boundary layers. Clauser (1954) showed that by balancing the shear stress contribution to growth of the momentum deficit with the pressure gradient contribution, boundary layers could be developed which exhibited similar velocity defect profiles. The velocity defect is defined as  $\bar{U} - U_e$  and is normalized with the shear velocity. This condition is satisfied in a boundary layer when the equilibrium parameter,  $\beta$ , as defined below, remains constant.

$$\beta = \frac{\delta^*}{\tau_w} \frac{dP}{dx} \quad (2.2)$$

It is very difficult to set the flexible wall to a shape which will produce this condition by trial and error as Clauser (1954) noted. Therefore, a technique was developed which used the two dimensional boundary layer code of Cebeci and Bradshaw (1977) to solve iteratively for a wall shape that would yield an equilibrium boundary layer. Here this computer program is called CBTSL. Ordinarily the code is used when the free stream variation of velocity over a surface is known, and one wishes to determine how the boundary layer develops over that surface. The free stream velocity is provided as an input at each x-location where one wishes an output to determine the nature of the boundary layer. The present technique uses the code as a tool to solve for the variation of free stream velocity necessary to develop an equilibrium boundary layer. Then based on the channel geometry, and the calculated displacement thickness, a wall shape is determined. The technique involves starting with an arbitrary variation of free stream velocity with streamwise distance. The boundary layer parameters are calculated by CBTSL, and then  $\beta$  is calculated for each x-location. A computational scheme, described below, then varies the free stream velocity repetitively until the equilibrium parameter is the same at each location. Computationally, the only downstream point in the CBTSL calculation which has an

influence on the flow parameters at a particular point is the downstream point closest to it. In other words, if the most upstream point in the calculation is  $i = 1$  and the most downstream point is  $i = N$ , then the only downstream point which has any effect on a given point  $i$  is the point  $i + 1$ . Thus to solve for a given value of  $\beta$  at point  $i$ , one must simply vary the value of the freestream velocity  $U_e$  at the point  $i + 1$  until the value of  $\beta$  at  $i$  reaches the desired value. This can be done in a systematic way in which  $U_e$  at  $i + 1$  is solved for iteratively using the secant method. At each iteration the code CBTSL is used to determine the necessary boundary layer parameters to calculate  $\beta$ . When the value of  $U_e$  at  $i + 1$  is found which gives the desired value of  $\beta$  at  $i$ , the process is repeated to determine the value of  $U_e$  at the point  $i + 2$  to achieve the desired value of  $\beta$  at the point  $i + 1$ . The process is repeated at each subsequent point until  $\beta$  is a constant for all points in the calculation. Once this is completed, the wall shape is calculated using the known channel geometry and the calculated value of the displacement thickness.

This technique did not take into account any three-dimensional effects such as corner flows. For this reason it was not expected that the calculated wall shape would yield an equilibrium boundary layer on the first attempt. It was, however, hoped that the wall shape determined using the calculation would make the procedure of obtaining equilibrium boundary layers much easier than the experience had by those who have generated such layers without the benefit of such calculations.

The procedure used to set the wall shape was as follows. First the wall was set to the shape determined by the calculation. Then the variation of freestream velocity was checked by making LDV measurements in the free stream at each measuring location. These measurements were checked against the free stream velocity variation determined in the calculation. If the measured free stream velocity variation was not within a few percent of the calculated velocity variation, the wall shape was changed slightly and the velocity measurements were repeated. This process was repeated until the  $U_e$  measurements

matched the calculation. After this, it was necessary to perform velocity traverses of the boundary layer at each measuring station to determine the displacement thickness and the shear velocity. The equilibrium parameter,  $\beta$ , was then calculated for each measuring location. These values were checked to insure that  $\beta$  did not vary by more than  $\pm 10\%$  from station to station. As a further check, velocity defect profiles were plotted to see if similar profiles existed. When this was not the case the wall shape was changed slightly, and the process was repeated. Happily, no more than two iterations were required to obtain the desired equilibrium boundary layers.

It is important to note that a serious limitation exists in the two dimensional calculation when it is applied to the internal flow geometry found in this test facility. Originally the two flows which were to be studied had values of  $\beta$  equal to 0.9 and 3.6. Nothing in the calculation indicated that the  $\beta = 3.6$  flow would separate. Nevertheless, injection of dye in the corners indicated that the flow was stalling in the corners on the flexible wall side of the channel. Further experimental iteration showed that a  $\beta$  value of less than approximately 2.0 was necessary to avoid separation in the corners. Thus the range of  $\beta$  values studied was reduced because of these three-dimensional effects in the corners.

It is possible to treat the test section as a diffuser to determine if diffuser stall prediction techniques will predict this stall. With a diffuser half angle of approximately  $4^\circ$ , the prediction technique of Reneau (1967), for two-dimensional diffusers, predicts "no appreciable stall" for the  $\beta = 3.6$  wall shape. "No appreciable stall", as defined by Reneau (1967), does allow for small areas of separation in the corners. While this definition of stalling is quite adequate for diffusers, it is not useful for the study of turbulent structures in an equilibrium adverse pressure gradient boundary layer facility. It would be nearly impossible to distinguish between flow oscillations due to unsteady separation, and normal turbulent fluctuations.

In order to study stronger pressure gradients in the facility, several modifications could be made to the channel. The easiest modification would be to shorten the distance over which the pressure gradient is applied. This would have the disadvantage of limiting the distance over which an equilibrium boundary layer could be maintained. Another method which shows the most promise of success is to bleed off small amounts of fluid from the corners next to the flexible wall. Since these experiments were performed by the author, Koskie (1989) has been able to obtain a  $\beta = 3.6$  flow, in the same boundary layer facility, with no separation by bleeding off fluid from the corners just upstream of the separation location.

## CHAPTER THREE - RESULTS

### 3.1 Evaluation of Shear Velocity

The shear velocity is used to normalize most of the of the important quantities measured in this study. Thus it is very important to obtain a very accurate estimate of the shear stress. For the case of zero pressure gradient boundary layers it has been shown by Coles (1968) that accurate estimates of shear velocity can be made by numerically iterating to solve equation 3.1, which is valid in the logarithmic or overlap zone, at each  $y$  location in the flow for the shear velocity,  $u_\tau$ . In this method the values of  $\kappa$  and  $B$  are assumed to be 0.41 and 5.0 (or 0.40 and 5.5) respectively (Coles 1968).

$$U^+ = \frac{1}{\kappa} \ln y^+ + B \quad (3.1)$$

where  $U^+$  is defined as:

$$U^+ = \frac{\bar{U}}{u_\tau} \quad (3.2)$$

and  $y^+$  is defined as:

$$y^+ = \frac{y u_\tau}{\nu} \quad (3.3)$$

This yields a region for which the calculated value of  $u_\tau$  is independent of the value of  $y$  as shown in figure 3.1. The value of  $u_\tau$  in this region is the value used as the estimate for shear velocity. For zero pressure gradient flows the values for  $\kappa$ , the von Karman constant, and  $B$ , the intercept, are well accepted to be 0.41 and 5.0 respectively (Coles 1968). Thus this is a simple method for finding the wall shear stress in a flat

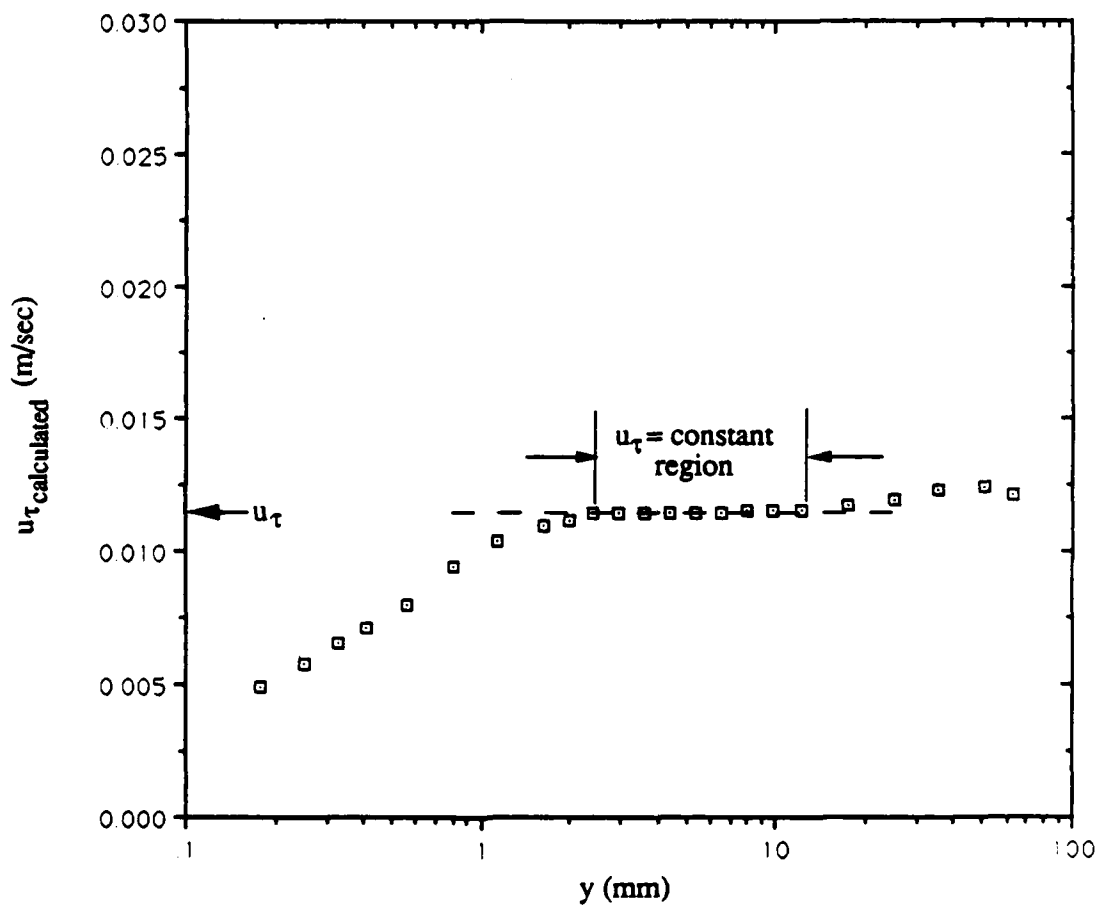


Figure 3.1. Calculated shear velocity for zero pressure gradient flow,  $R_{\theta} = 1530$ :  $\square$ ,  $u_{\tau \text{ calculated}}$ ; — — — —,  $u_{\tau \text{ mean}}$ .

plate flow. Although many investigators (Coles 1968) have used equation 3.1 to solve for the shear velocity in non-zero pressure gradient flows, it is not clear that the values of the constants in equation 3.1 remain the same in non-zero pressure gradient flows. Therefore, a method is needed that does not require prior knowledge of the constants in the law of the wall equation.

One of the advantages of the very thick boundary layers developed in this low speed water flow is that the viscous sublayer is sufficiently thick to allow accurate measurements for  $y^+$  locations as low as 2 or 3. For  $y^+$  locations less than 6, the velocity follows the behavior:

$$U^+ = y^+ \quad (3.4)$$

Thus the velocity profile in the viscous sublayer is linear, and the shear velocity can be defined as:

$$u_\tau^2 = \nu \frac{d\bar{U}}{dy} \quad (3.5)$$

Using velocity data at two different  $y$  locations in the sublayer, this equation can be solved for  $u_\tau$ . This method is often referred to as the wall slope method. Figure 3.2 shows graphically how  $u_\tau$  is determined from the near wall velocity data. Because of the relatively large dimensions of the sublayer an uncertainty analysis showed that the shear velocity could be estimated to within  $\pm 4\%$  for the zero pressure gradient flow and even more accurately in the thicker sublayers of the two adverse pressure gradient flows. A detailed discussion of the uncertainty analysis is given in Appendix A.2. Although the distance between  $y$  locations in the sublayer could be accurately determined, the absolute distance from the wall was subject to greater uncertainty. For this reason the  $y$  values for the data taken in the sublayer were corrected so that a line passing through these points would also pass through the origin. Then the absolute value of  $y$  was checked for all points used to calculate the shear velocity to insure that only  $y^+$  values less than 6 were used. It is interesting to note that for all but two measuring locations in the non-zero pressure gradient

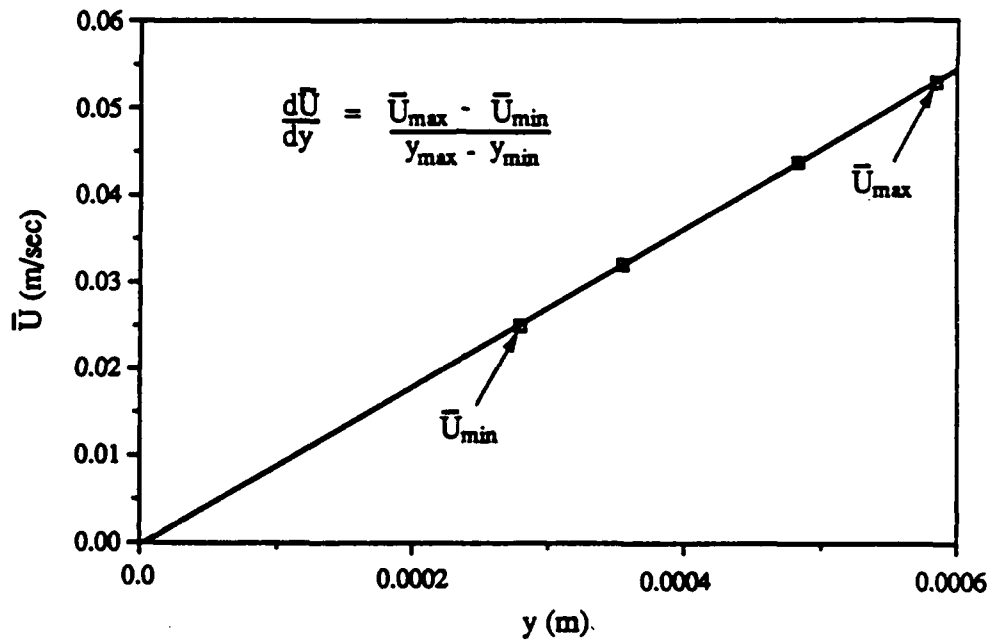


Figure 3.2 Linear velocity profile in the viscous sublayer.

flows the value calculated from the wall slope method was within 2% of the value found using the law of the wall method. The law of the wall method was used for calculating shear velocity for the zero pressure gradient case to allow for better comparison with data from other investigators. The wall slope method was used for calculating shear velocity for the adverse pressure gradient cases. Table 3.1 shows the value of  $u_\tau$  calculated using each method and the method of Coles (1968), which is a correlation based on momentum thickness Reynold's number and shape factor. Note that the shear velocity calculated using Coles method was consistently lower than either the law of the wall method or the wall slope method.

Table 3.1 - Shear velocity (mm/sec) calculated using three methods

$\beta$	$x$ (cm)	$Re_\theta$	<u>wall-slope</u>	<u>law-of-wall</u>	<u>Coles</u>
0.0	38.5	1120	11.8	12.0	11.2
0.0	65.6	1260	11.6	11.8	11.0
0.0	90.1	1410	11.5	11.7	11.0
0.0	124.5	1540	11.1	11.4	11.0
0.8	38.0	1265	10.4	10.4	9.8
0.8	66.5	1530	9.4	9.4	8.9
0.7	90.0	1780	9.1	9.1	8.6
0.8	125.0	2090	8.5	8.6	8.1
1.7	38.1	1315	8.8	9.4	9.0
1.8	65.2	1796	8.4	8.0	7.7
1.8	90.0	2085	7.6	7.5	7.1
1.7	124.3	2495	7.0	6.9	6.6

### 3.2 Zero Pressure Gradient Flow

Zero pressure gradient measurements were made at each of four measuring locations. These locations were at  $x = 38.1$  cm, 66.5 cm, 90.0 cm, and 124.5 cm where  $x$  is measured from the trip location. The Reynolds number based on the momentum thickness at each location was  $R_\theta = 1120, 1260, 1410$  and 1540 respectively. These measurements were made to verify the standard nature of the flow and to provide a comparison with the non-zero pressure gradient flows. The zero pressure gradient case has been well studied by many other experimenters. Clauser (1954) performed mean flow measurements in a boundary layer wind tunnel. Murlis, Tsai and Bradshaw (1982) measured the turbulent structure of boundary layers at low Reynolds numbers in the range of the present study. Spalart (1988) performed a numerical simulation of a zero pressure gradient boundary layer at various low Reynolds numbers. Purtell, Klebanoff and Buckley (1981) performed measurements in zero pressure gradient boundary layers at higher Reynolds numbers than those in the present study.

#### 3.2.1 Mean Velocity Profiles

Figure 3.3 shows the mean velocity profiles from the four measuring stations in the zero pressure gradient flow. The velocity is normalized with the shear velocity and the  $y$  location is normalized with the shear velocity and the kinematic viscosity. As can be seen, these data follow closely equation 3.2 in the sublayer, and there is a linear region for which equation 3.1 fits very well. This indicates that the values of  $\kappa = 0.41$  and  $B = 5.0$  are correct for this zero pressure gradient flow. To verify the standard nature of the flow, figure 3.4 shows the mean velocity profile at the third measuring location which corresponds to  $R_\theta = 1410$ . Also shown in this plot is the calculated velocity profile from Spalart's (1988) direct simulation at  $R_\theta = 1410$  and data from Murlis *et al.* (1982) at  $R_\theta = 1368$ . The data follow Spalart's simulation nicely and serve to verify the calculation. Clauser (1954) showed that for velocity data in an equilibrium boundary layer,  $\beta = 0$  being

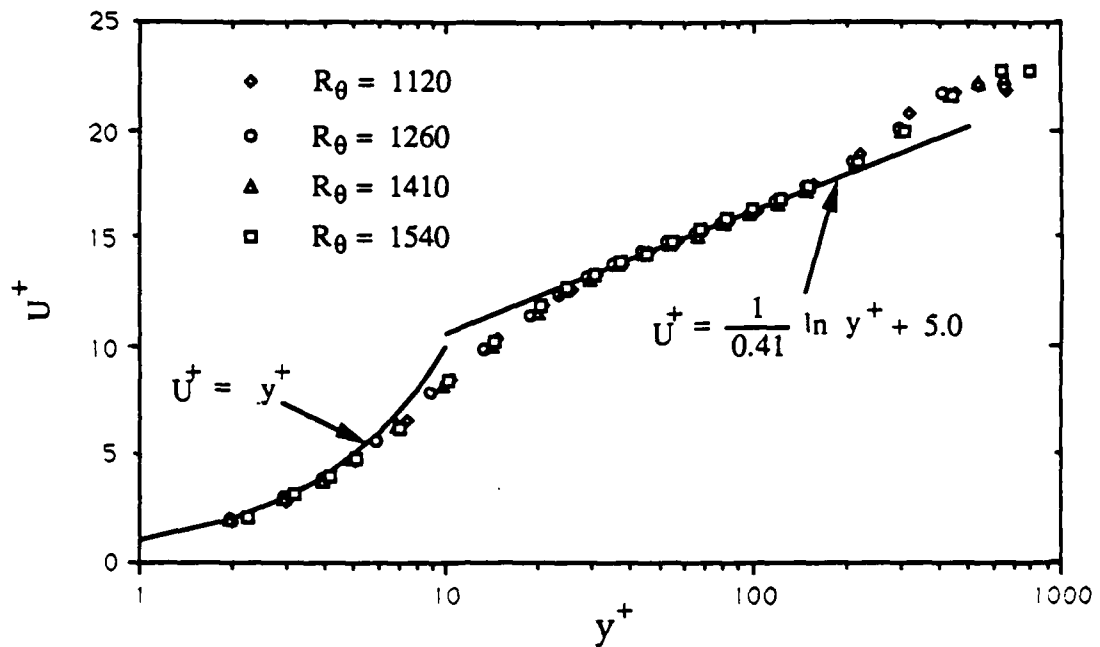


Figure 3.3. Mean velocity profiles for zero pressure gradient flow.

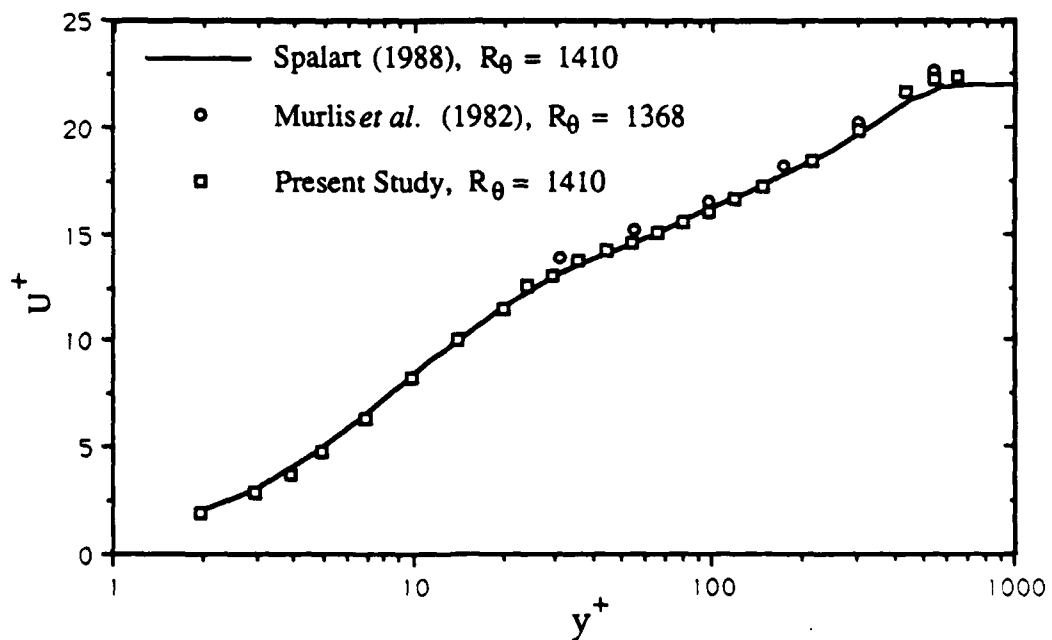


Figure 3.4. Comparison of mean velocity profile at  $R_\theta = 1410$ .

the simplest case, a plot of the velocity defect,  $\bar{U} - U_e$ , normalized with shear velocity versus  $y$  normalized with the Clauser thickness  $\Delta$  where

$$\Delta = \delta^* \frac{U_e}{u_\tau} \quad (3.6)$$

would form a universal profile. Figure 3.5 shows the velocity defect profiles for each measuring location plotted with the defect profile for zero pressure gradient from Clauser (1954). These comparisons verify the present flow as a valid zero pressure gradient boundary layer. It was also necessary to verify that the boundary layer was two dimensional. This was done by measuring the velocity profiles from the first and last stations at a  $z$  location off-set from the channel center. These measurements were performed at  $z = 10.2$  cm (the center of the wall is at  $z = 20.4$  cm) and by symmetry show that over the central 20.4 cm the boundary layer is two dimensional. These two dimensionality profiles are shown in appendix A.1.

### 3.2.2 RMS of Streamwise Velocity

Figure 3.6 shows root-mean-square (RMS) of the fluctuating streamwise velocity as a function of distance from the wall for each measuring station. These results show that for all the zero pressure gradient cases,  $u'^+$  peaks at  $y^+ \approx 14$ . For the lowest Reynolds number,  $R_\theta = 1120$ ,  $u'^+$  peaks at 2.59. For the remaining three cases,  $u'^+ \approx 2.65$  at the peak. The data show good agreement with the  $u'^+$  data from Erm *et al.* (1985) at  $R_\theta = 1359$  down to  $y^+ = 30$ . Figure 3.7 shows that the data at  $R_\theta = 1410$  match very well in the near wall region,  $y^+ < 30$ , with the calculation from Spalart (1988) at the same Reynolds number. Note that the  $u'^+$  data collapse (see figure 3.6) for  $y^+$  less than 50, verifying that normalization with "inner variables" is correct for the near wall region. The data compare fairly well with Purtell *et al.* (1981) for  $y^+$  less than 30. The effect of the larger Reynolds number is quite evident at larger  $y^+$  values

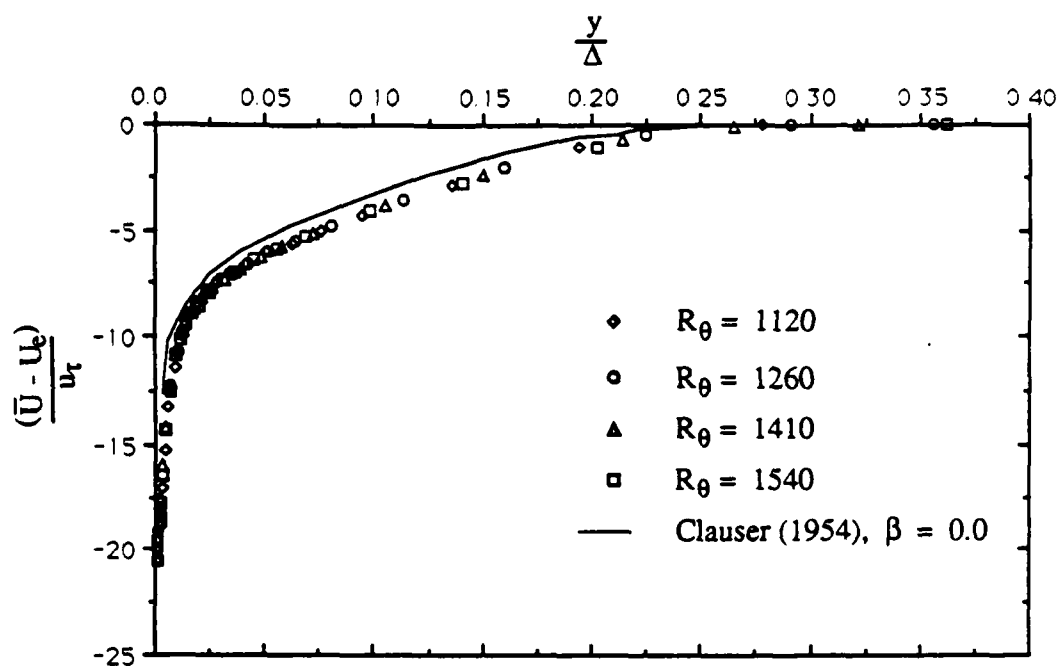


Figure 3.5. Velocity defect profiles for zero pressure gradient boundary layer.

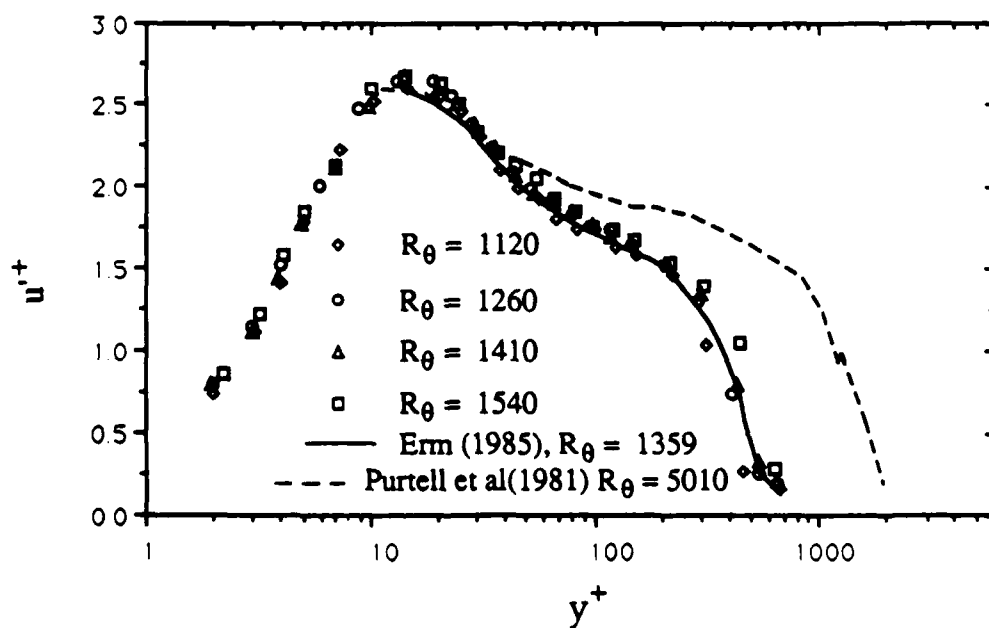


Figure 3.6. RMS of streamwise velocity for zero pressure gradient flow.

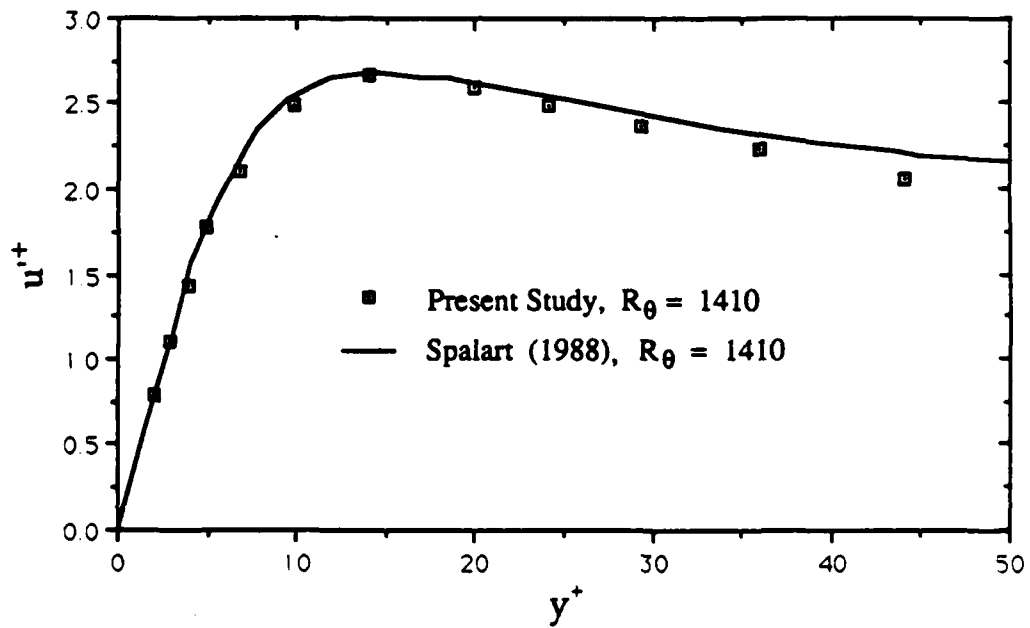


Figure 3.7. RMS of streamwise velocity for zero pressure gradient at  $R_{\theta} = 1410$ .

### 3.3 Mild Adverse Pressure Gradient Flow

The mild adverse pressure gradient flow was an equilibrium boundary layer with  $\beta = 0.8$ . Although this is a fairly mild pressure gradient it did lead to a significant reduction in the wall shear stress at each of the measuring locations. Measurements were made at  $x = 38.1$  cm, 66.5 cm, 90.0 cm, and 125.0 cm. The Reynolds number based on the momentum thickness at each location were  $R_{\theta} = 1265, 1530, 1780$  and 2090 respectively. This yielded K values between  $K = -0.38 \times 10^{-6}$  and  $K = -0.52 \times 10^{-6}$ , where K is defined as:

$$K = \frac{v}{U_e^2} \frac{d\bar{U}_e}{dx}$$

#### 3.3.1 Mean Velocity Profiles

Figure 3.8 shows the mean velocity profiles for each measuring location in the  $\beta = 0.8$  boundary layer. One can see that although the data fit fairly well to equation 3.1 with the constants as used with the zero pressure gradient case, there appears to be a slight difference in the slope and intercept for some of the data. This variation is discussed in greater detail in section 3.5. The velocity defect profiles in Figure 3.9 are important to show that the boundary layer is indeed in equilibrium. Clauser (1954) showed that the velocity defect profiles will form similar profiles only when the pressure gradient contribution to the growth of the momentum deficit is kept a constant multiple of the shear stress contribution. This condition is satisfied when  $\beta = \text{constant}$ . Figure 3.9 shows the data from each station falling neatly onto one curve. This gives a good indication that the boundary layer is truly in equilibrium. As with the zero pressure gradient case, two dimensionality was verified by performing velocity traverses at a z location offset from the center of the wall. Figures showing the degree of two dimensionality can be found in Appendix A.2.

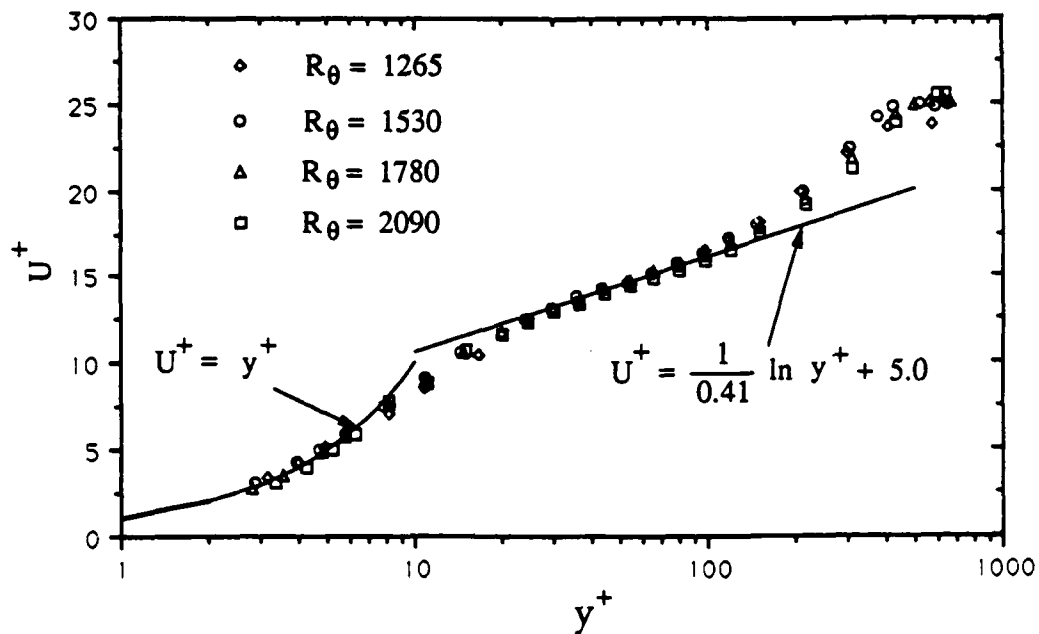


Figure 3.8. Mean velocity profiles for mild pressure gradient boundary layer.

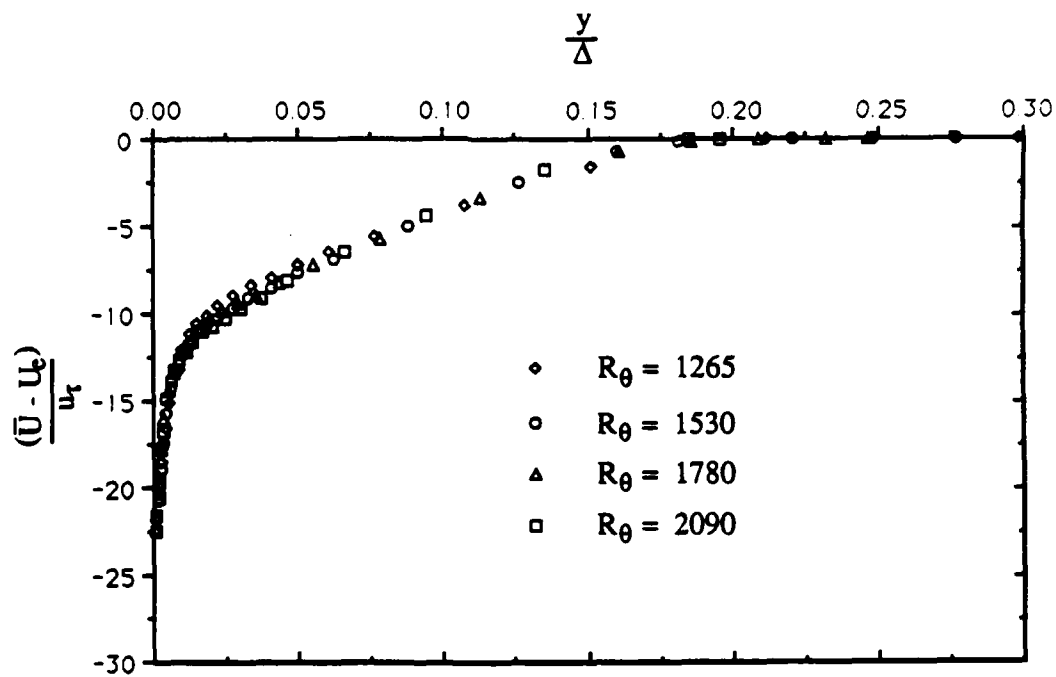


Figure 3.9. Velocity defect profiles for mild pressure gradient boundary layer

### 3.3.2 RMS of Streamwise Velocity

Figure 3.10 shows the RMS of the fluctuating streamwise velocity as a function of distance from the wall for each measuring location. The  $y^+$  location for the  $u'^+$  peak occurs at  $y^+ \approx 15$ . The value of this peak is  $u'^+ \approx 2.84$ . From this it can be seen that the location of the  $u'^+$  peak remains approximately the same as for the zero pressure gradient case, but the level of the  $u'^+$  peak has increased. In the region of  $y^+ < 80$  the data follow basically the same curve, showing that  $u'$  scales with the inner variables in this region just as with the zero pressure gradient case. At higher values of  $y^+$  the data begin to diverge. Upon examination it can be seen that this variation is a function of Reynolds number. Wei and Willmarth (1989) show that the fluctuating quantities in the outer region do not scale with the inner variables and that there is a Reynolds number dependence. Harder (1989) noted this Reynolds number dependence also. Unlike Wei and Willmarth (1989), Harder (1989) also noted that inner variable scaling collapsed the  $u'$  data in the near wall region.

### 3.4 Strong Adverse Pressure Gradient

Figure 3.11 shows the mean velocity profiles for the strong adverse pressure gradient boundary layer in which  $\beta \approx 1.8$ . Measurements were made at  $x = 38.0$  cm, 65.4 cm, 90.0 cm, and 124.5 cm. The Reynolds number based on the momentum thickness at each location were  $R_{\theta} = 1315, 1796, 2085$  and 2495 respectively. The velocity data vary significantly from the zero pressure gradient profile in the logarithmic region. The profile at the first measuring location varies significantly from the profile shapes found at the three downstream locations. This is the only location where the shear velocity calculated from the law of the wall method varies by more than 5% from the value of shear velocity calculated using the wall slope method. The law of the wall method may fail at this location because it is only a short distance downstream from where the strong pressure gradient has been suddenly applied to the flow. The boundary layer profile may still be in a state of transition in which the velocity in the logarithmic zone is not a function of the local shear

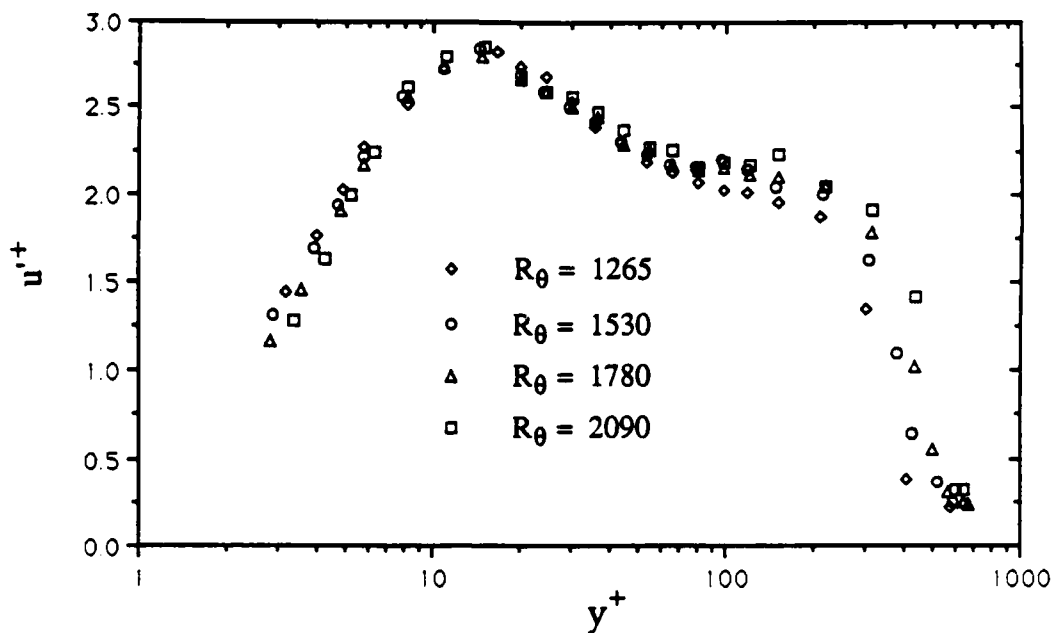


Figure 3.10. RMS of streamwise velocity for mild pressure gradient flow.

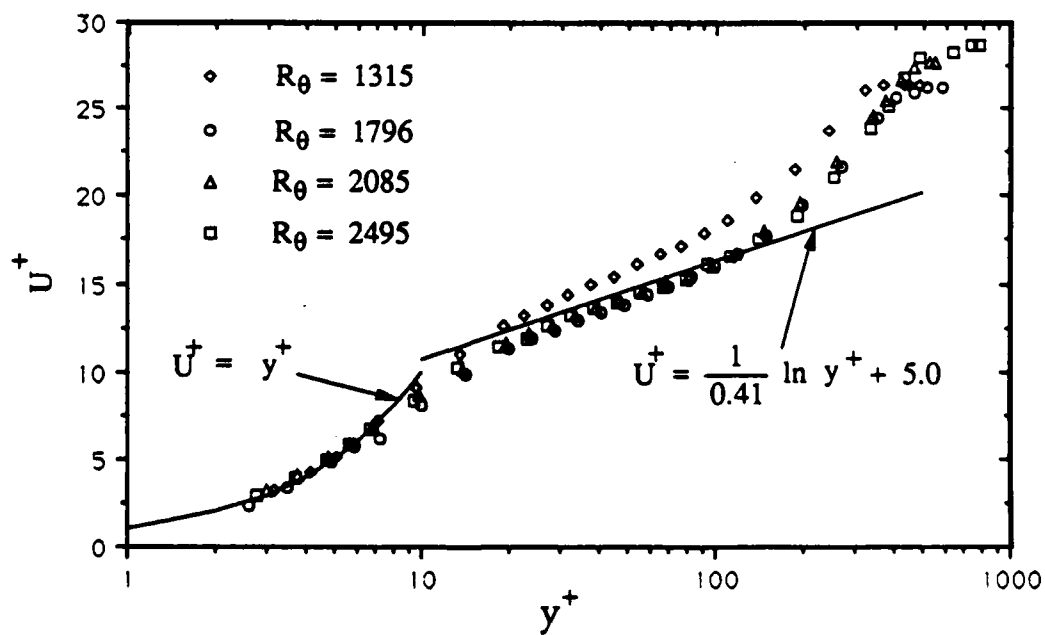


Figure 3.11. Mean velocity profiles for strong adverse pressure gradient flow.

stress. The data indicate that, for flow cases in the range of pressure gradient found in this study, the law of the wall method may be a very adequate method for calculating shear velocity. This is of course with the exception of sudden changes in the pressure gradient as in the case of a suddenly applied pressure gradient. White (1974) noted that methods for calculating wall shear stress which rely on the law of the wall are generally accurate except where sudden changes in the pressure gradient occur such as in the case of a relaxing flow. Although it is possible to obtain a reasonable estimate of shear velocity in the three downstream locations, using the zero pressure gradient values of  $\kappa$  and  $B$ , it is obvious that the velocity data vary significantly from equation 3.1 using  $\kappa = 0.41$  and  $B = 5.0$ . This indicates that the adverse pressure gradient alters the values of  $\kappa$  and  $B$ . This variation of  $\kappa$  and  $B$  with pressure gradient is discussed in section 3.5.

#### 3.4.1 Mean Velocity Profiles

As seen in figure 3.11 the velocity profiles at the last three measuring locations conform to the general behavior of the zero and mild pressure gradient flows. However, the slope and intercept for the linear logarithmic region change. Figure 3.12 shows the velocity defect profiles for the strong adverse pressure gradient,  $\beta = 1.8$ , flow. The profiles for the last three stations generally follow the same profile shape. These data follow closely to the curve which represents the velocity defect profile from the Clauser (1954)  $\beta = 1.8$  flow. The first profile does not conform to this profile shape in spite of the fact that the calculated value for  $\beta$  at this location is 1.84. This can be explained by the fact that the upstream history to this point is definitely not an equilibrium flow, and the velocity profile requires time to adjust to the equilibrium profile. For this reason the data from the first measuring location in each of the three flows is used only for defining the upstream history for the second measuring station and no burst structure information was measured there.

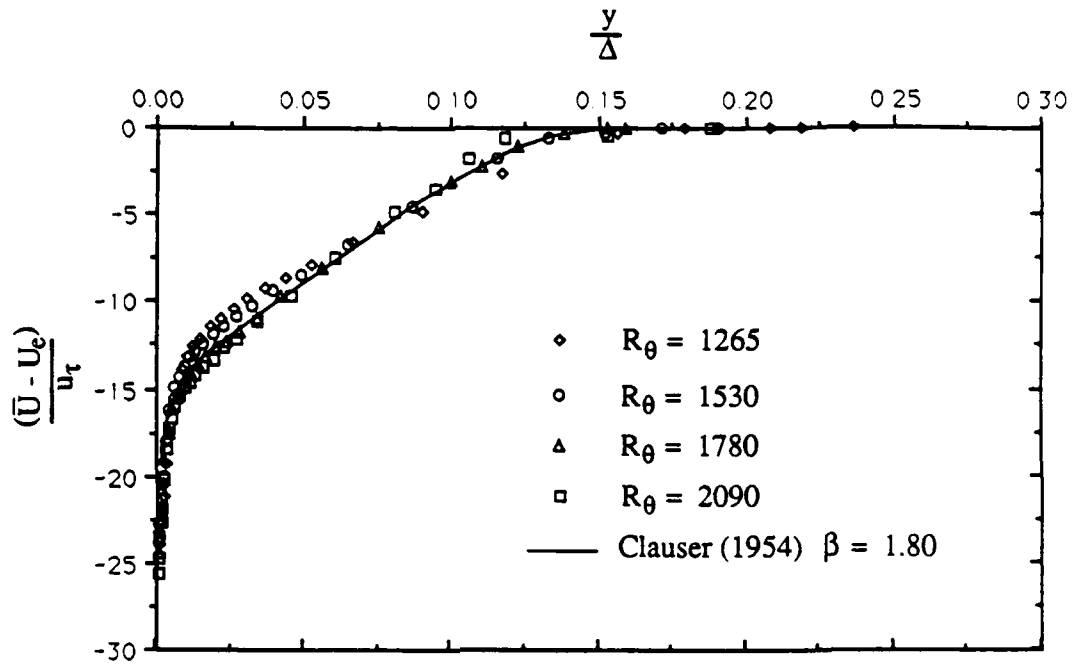


Figure 3.12. Velocity defect profiles for strong adverse pressure gradient flow.

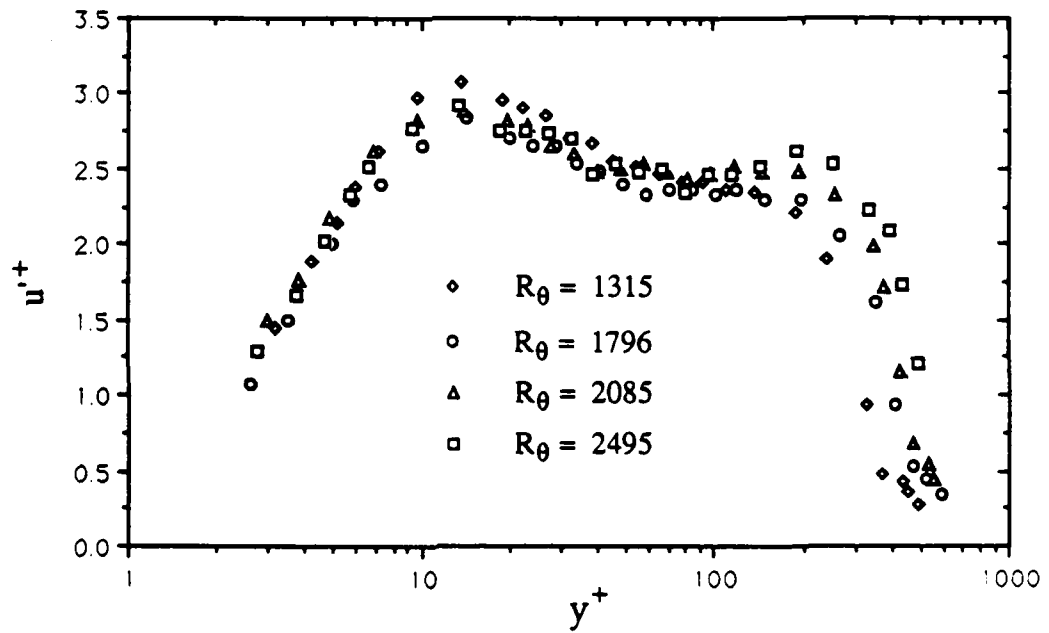


Figure 3.13. RMS of streamwise velocity for strong adverse pressure gradient flow.

### 3.4.2 RMS of Streamwise velocity

Figure 3.13 shows the RMS of the fluctuating streamwise velocity as a function of the distance from the wall for the strong adverse pressure gradient case. The RMS profiles for the last three stations follow approximately the same profile for  $y^+ < 80$ . As with the mean velocity profile for this case, the values of  $u^+$  are higher at the first measuring station. The peak in  $u^+$  appears to occur at  $y \approx 14$ . The peak value of  $u^+$  was equal to  $u^+ \approx 2.90$  for the last three stations and  $u^+ \approx 3.08$  for the first measuring station. An interesting feature of the  $u^+$  profiles is that as the Reynolds number increases a second peak begins to appear at  $y^+ \approx 110$ .

### 3.5 Variation of the von Kaman Constant and the Intercept

In order to determine the effect of the adverse pressure gradient on the value of the von Karman constant and the intercept, a logarithmic least squares fit of the data in the logarithmic region was performed. Coles (1968) chose which points to include in a fit of the logarithmic region by inspecting large number of velocity profiles from many different flows and determining a range of  $y^+$  values for which all the profiles exhibited logarithmic behavior. For the large Reynolds number flows studied by Coles, this region was determined to be  $100 \geq y^+ \geq 300$ . For the low Reynolds number flows in the present study, this is obviously not the proper choice. Examination of the velocity profiles reveals that the logarithmic region is in the region of  $30 \leq y^+ \leq 100$ . Thus to determine the values of the von Karman constant and intercept for each flow, a logarithmic least squares fit of the data points in the region of  $30 \leq y^+ \leq 100$  was performed. Table 3.2 show the values of  $\kappa$  and  $B$  obtained from this fitting process.

The von Karman constant varies from the accepted value of 0.41 by as much as 7% in the zero pressure gradient case and the value of the intercept varies by as much as 16%. These variations follow no clear Reynolds number trend, and therefore indicate the

uncertainty associated with the estimate of these constants. The values of the von Karman constant for the adverse pressure cases vary by less than 10% from the zero pressure gradient value and the value of the intercept varies from the zero pressure gradient value by less than 14%, with the exception of the data from the first measuring location for both adverse pressure gradient flows and the second measuring location for the strong adverse pressure gradient case. The large difference between the value of the von Karman constant and intercept determined at these measuring locations for both adverse pressure gradient flows is likely to be due to the sudden change in the pressure gradient which occurred just upstream of the first measuring location. This effect may not have completely disappeared at the second measuring location in the strong adverse case. Other than at the first measuring location in the mild adverse case, the von Karman constant and intercept appear, for the mild adverse case, to be equal the zero pressure gradient values to within the uncertainty expected based on the zero pressure gradient results. This also appears to be the case for the last two measuring locations in the strong adverse case.

Table 3.2 - Von Karman constant and intercept

$\beta$	$x$ (cm)	$Re_\theta$	$\kappa$	$B$
0.0	38.5	1120	0.41	4.9
0.0	65.6	1260	0.44	5.8
0.0	90.1	1410	0.43	5.5
0.0	124.5	1540	0.40	4.7
0.8	38.0	1265	0.35	3.3
0.8	66.5	1530	0.41	5.0
0.7	90.0	1780	0.39	4.4
0.8	125.0	2090	0.41	4.8
1.7	38.1	1315	0.31	3.2
1.8	65.2	1796	0.37	3.3
1.8	90.0	2085	0.40	4.3
1.7	124.3	2495	0.43	5.0

### 3.6 Turbulent Burst Structure

Real-time velocity records of at least 1000 burst periods are necessary to provide reliable information on the period of the burst cycle. In order to provide an accurate real-time velocity record, data was acquired at a rate equal to or greater than the viscous frequency given by  $u_{\tau}^2/\nu$ . The data acquisition system was configured such that a velocity word and a time word were simultaneously acquired. Since this study involved measurements of the streamwise velocity only, the modified u-level technique of Luchik and Tiederman (1987) was used for ejection detection.

#### 3.6.1 Burst Detection Technique

The modified u-level technique is a very simple technique which takes advantage of the significant drop in free stream velocity which occurs as an ejection passes through the detector. The detector is turned on when

$$u < -Lu' \quad (3.7)$$

and turned off again when

$$u \geq -0.25Lu' \quad (3.8)$$

where  $u$  is the fluctuating streamwise velocity,  $L$  is the threshold and  $u'$  is the streamwise RMS velocity.

This and other such detection techniques detect ejections. A burst can consist of more than one ejection and it is therefore necessary to group the ejections into individual bursts in order to determine the period of the burst cycle. This is done by determining a grouping parameter which is simply a time increment. Any ejections occurring within that time increment are considered to be from the same burst and are grouped as such. This grouping parameter is found using a probability plot of the time between ejections as shown in figure 3.14. The plot consists of three approximately straight line regions. The first region involves ejections from the same burst. The third region involves ejections from different bursts. The middle region is an over-lap region which involves a mixture of ejections from the same burst and ejections from different bursts. The center of the over-

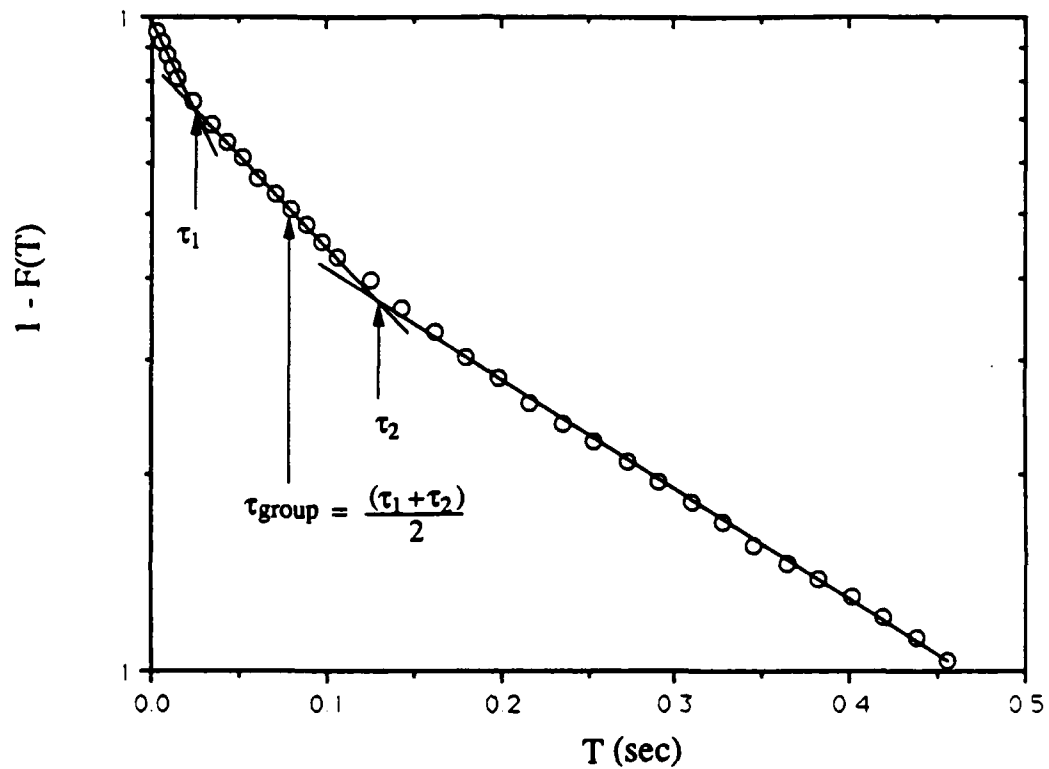


Figure 3.14. Probability plot for time between ejections. Zero pressure gradient flow,  $R_\theta = 1540$ ,  $L = 0.60$ .

lap region is defined as the grouping parameter. Since the grouping parameter cannot be determined exactly, twenty-five percent of the range of region two on either side of the grouping parameter is assigned as the region of uncertainty for the grouping parameter. The center of the over-lap region is determined by making a least squares fit to the data in each of the three regions and then taking the center to be the point half way between the intersections formed by these three lines. The detector function must be used over a range of thresholds and the grouping parameter is found for each threshold separately. A range must be found for which the burst period is independent of the threshold. In figure 3.15 we see the burst period,  $\bar{T}_b$ , plotted as a function of threshold. The value of  $\bar{T}_b$  is then defined as the value of  $\bar{T}_b$  in the threshold independent region. Luchik and Tiederman (1987) showed that the region of relative threshold independence often contains a slight minimum and proposed using this minimum value for  $\bar{T}_b$ . Thus in this analysis when such a minimum was present that value was taken as the average burst period.

### 3.6.2 Period of the Bursting Cycle

#### 3.6.2.1 Zero Pressure Gradient

A value of  $\bar{T}_b^+$  of order 100 is generally accepted to be valid over a wide range of Reynolds numbers for both zero pressure gradient and two dimensional channel flows. Recently, Harder (1989) found that  $\bar{T}_b^+ \approx 71$  for the two dimensional channel flows in his study when the burst period was normalized with the local shear velocity instead of the shear velocity based on pressure drop in the channel. Harder (1989) also noted that the channel flow data of Walker (1988) yielded this same lower value of  $\bar{T}_b^+$  when normalized with the local value of shear stress. In this study, a value of  $\bar{T}_b^+ \approx 67$  was

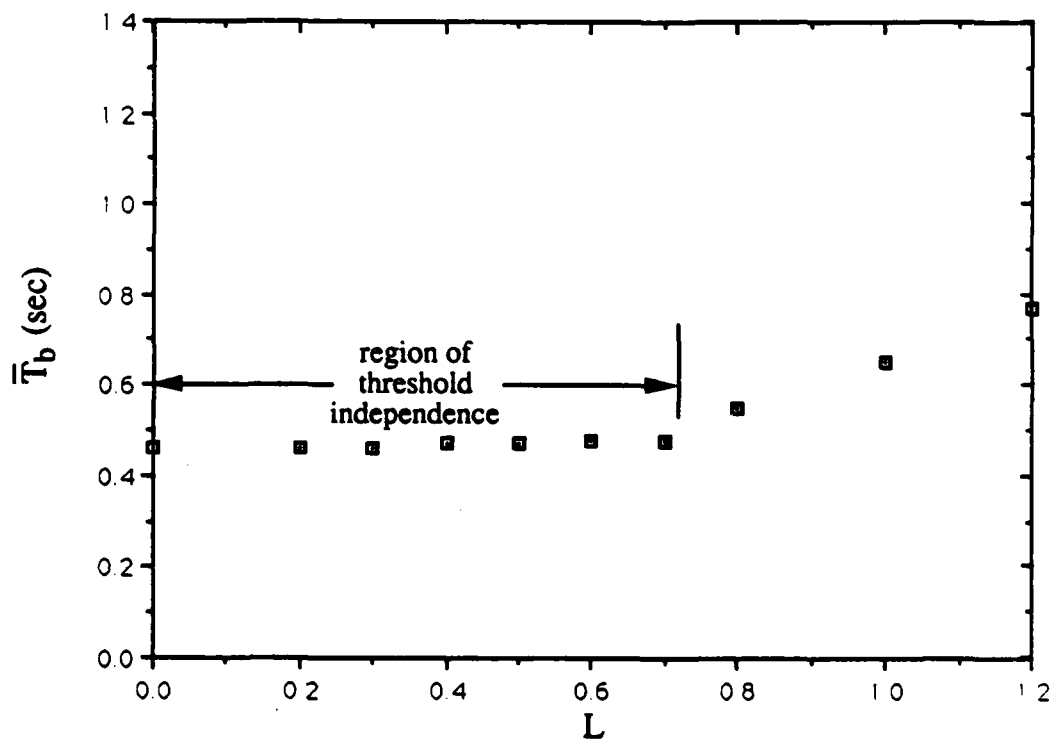


Figure 3.15. Period of the burst cycle,  $\bar{T}_b$ , as a function of threshold,  $L$ , for zero pressure gradient flow at  $R_\theta = 1540$ .

determined for the zero pressure gradient boundary layer. This value is significantly lower than that found by other investigators, with the exception of Harder (1989). Shah and Antonia (1988) found the value of  $\bar{T}_b^+ \approx 150$  for the zero pressure gradient boundary layer for  $2000 > R_0 > 6000$ . At present the explanation for this difference is not clear. It is most likely due to the method of grouping which was used. Shah and Antonia (1988) reported using the exponential technique for grouping ejections into bursts

Figure 3.16 shows the value of  $\bar{T}_b^+$  normalized with inner variables,  $\bar{T}_b^+$ , as a function of Reynolds number. Burst data are shown from each pressure gradient case. Data from Walker (1988), Luchik and Tiederman (1987) as renormalized by Harder (1989), and Harder (1989) show that for channel flows the value of  $\bar{T}_b^+$  is independent of Reynolds number over a wide range. Figure 3.16 indicates that over the limited Reynolds number range of this study, The value of  $\bar{T}_b^+$  is independent of Reynolds number to within the uncertainty in  $\bar{T}_b^+$  for each equilibrium flow. Figure 3.17 clearly indicates that  $\bar{T}_b^+$  is a function of the pressure gradient parameter  $\beta$ . The normalized burst period clearly decreases with increasing  $\beta$ . Finnicum and Hanratty (1988) proposed a model which described the variation of burst period,  $\bar{T}_b^+$ , with pressure gradient for favorable pressure gradients. This model proposes that the change in,  $\bar{T}_b^+$ , due to pressure gradient is inversely proportional to the pressure gradient,  $dP/dx$ , normalized with shear velocity and kinematic viscosity. This model yields an increasing value of,  $\bar{T}_b^+$ , as pressure gradient decreases (becomes more favorable). This behavior is also seen in the study of Simpson and Strickland (1977). Simpson and Strickland also showed that  $\bar{T}_b^+$  decreases with increasingly adverse pressure gradient. This result can serve only as a qualitative comparison to the present study because the burst period information was obtained using the short time autocorrelation technique which has not been verified as thoroughly as the modified u-level technique. Nonetheless, this trend is the same as that of the adverse pressure gradient flows in the present study. A linear model, which decreases with increasing pressure gradient, fits this data very well giving a correlation coefficient of 0.96.

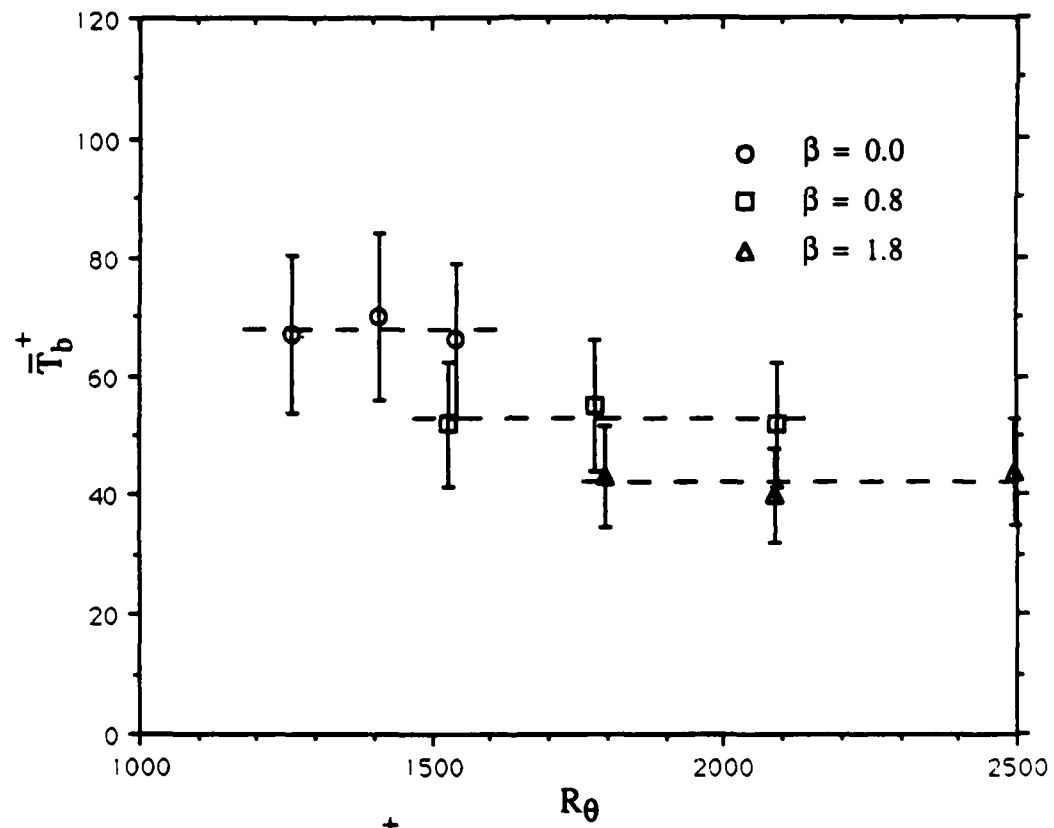


Figure 3.16. Burst period,  $\bar{T}_b^+$ , as a function of Reynolds number for all flows.

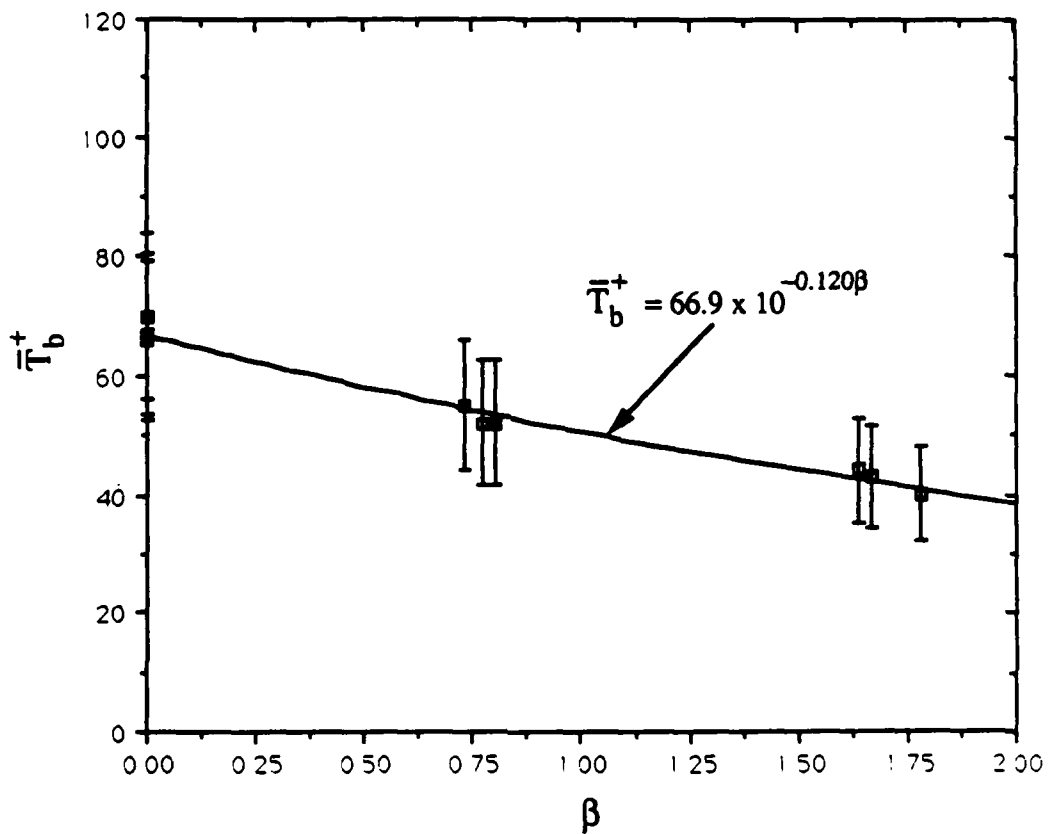


Figure 3.17. Normalized burst period,  $\bar{T}_b^+$ , as a function of the equilibrium parameter,  $\beta$ .

While this provides a means of estimating  $\bar{T}_b^+$  over the range of  $\beta$  values shown, it is not very satisfying physically. The linear variation of normalized burst period with  $\beta$  would indicate that  $\bar{T}_b^+$  becomes zero at  $\beta \approx 4.5$ . Thus an exponential fit was performed which yielded a correlation coefficient of 0.98. This model is given as:

$$\bar{T}_b^+ = 66.9 \times 10^{-0.120\beta} \quad (3.9)$$

Considering the 20% uncertainty in  $\bar{T}_b$ , this does not provide a significantly better estimate of  $\bar{T}_b$ , but it does allow for non-zero values of  $\bar{T}_b^+$  at values of  $\beta$  higher than 4.5. In figure 3.18 the normalized burst period has also been plotted as a function of  $G$ , the Clauser (1954) shape factor (see figure 3.18). Clauser noted that a shape factor which is constant in an equilibrium flow must be a function of shear velocity. He showed that in an equilibrium boundary layer

$$G = H \frac{U_e}{u_\tau} \quad (3.10)$$

should remain approximately constant. Thus  $G$  and  $\beta$  are intimately related and any quantity that is a function of one should be equally a function of the other. The exponential fit to the plot of  $\bar{T}_b^+$  versus  $G$  is given as:

$$\bar{T}_b^+ = 154 \times 10^{-0.0522G} \quad (3.11)$$

It has a correlation coefficient of 0.96. This is nearly as good a fit as the one involving the equilibrium parameter  $\beta$ . The benefit of knowing  $\bar{T}_b^+$  as a function of  $G$  is that an accurate estimate of  $U_e(x)$  is not required to estimate the burst period. Figure 3.19 shows  $\bar{T}_b^+$  as a function of  $K$  where  $K$  is defined as:

$$K = \frac{v}{U_e^2} \frac{dU_e}{dx} \quad (3.12)$$

This provides the model:

$$\bar{T}_b^+ = 70.5 + (32.2 \times 10^6)K \quad (3.13)$$

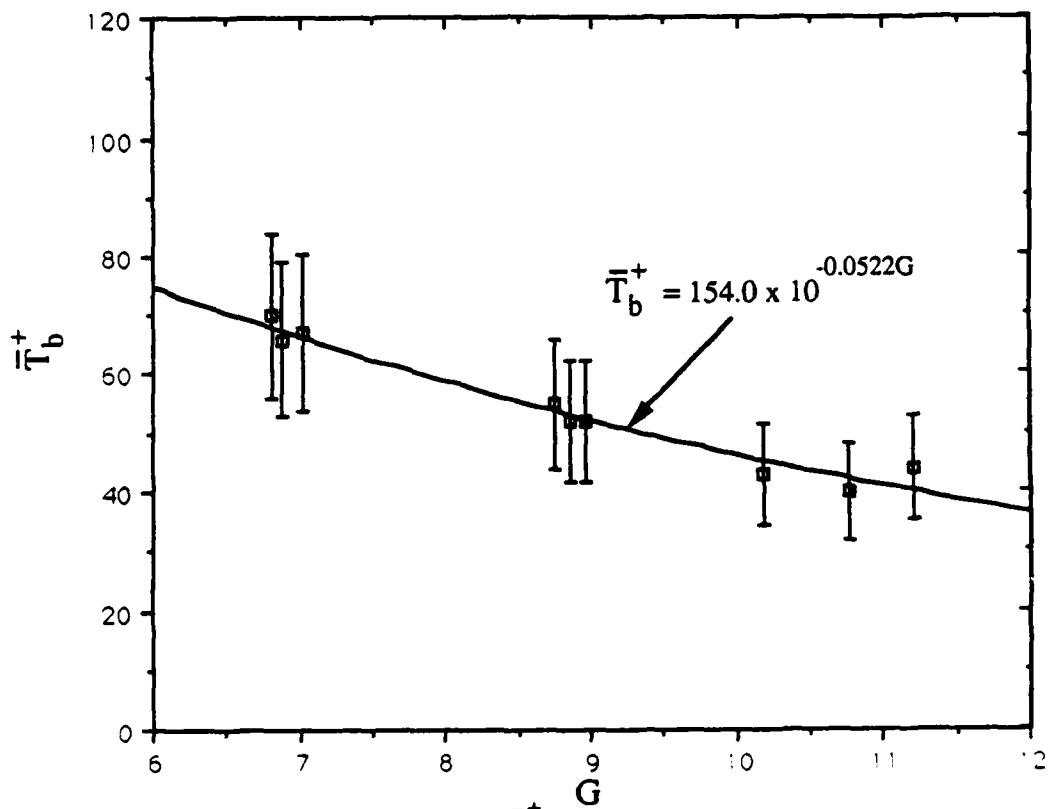


Figure 3.18. Normalized burst period,  $\bar{T}_b^+$ , as a function of the Clauser shape factor,  $G$ .

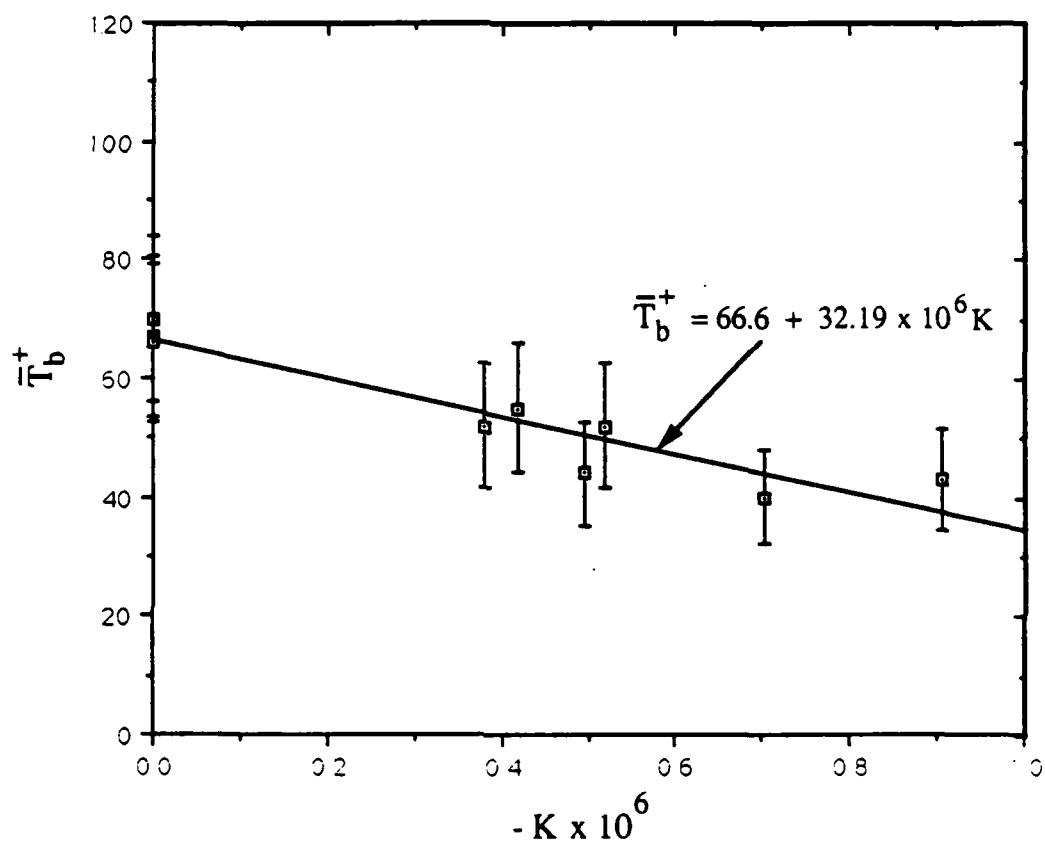


Figure 3.19. Normalized burst period,  $\bar{T}_b^+$ , as a function of the pressure gradient parameter,  $K$ .

which has a lower correlation coefficient of 0.85, but allows an estimate of  $\bar{T}_b^+$  to be made independent of the wall shear stress. The straight line fit was used because it allows for non-zero values of  $\bar{T}_b^+$  in the range of  $K$  for which separation of a two dimensional boundary layer does not occur. Note, however, that  $K$  does not take into account the upstream history of the boundary layer. Since the turbulent structure of a boundary layer is very much a function of its upstream history,  $K$  is not the ideal choice of independent variable with which to characterize the burst structure of a turbulent boundary layer.

### 3.6.2 Conditionally Sampled Velocities

Conditionally averaged streamwise velocity signals were analyzed to determine if the pressure gradient affected the shape of the "average" burst signal. Figure 3.20 shows a conditionally averaged signal from each pressure gradient centered on the burst leading edge. These signals are very similar in nature. The derivative of the ensemble averaged signal with respect to  $T^+$  is identical for all three cases at the leading edge of the burst. The sweeping motion which precedes the burst event seems to be slightly damped in the strong adverse pressure gradient case. With this exception, the pressure gradient seems to have little effect on the signal characteristics. The same is true in figure 3.21, except that the sweeping motion following the burst event is slightly damped for the strong adverse pressure gradient case. This indicates that the nature of the individual burst event is not significantly altered by presence of the adverse pressure gradient.

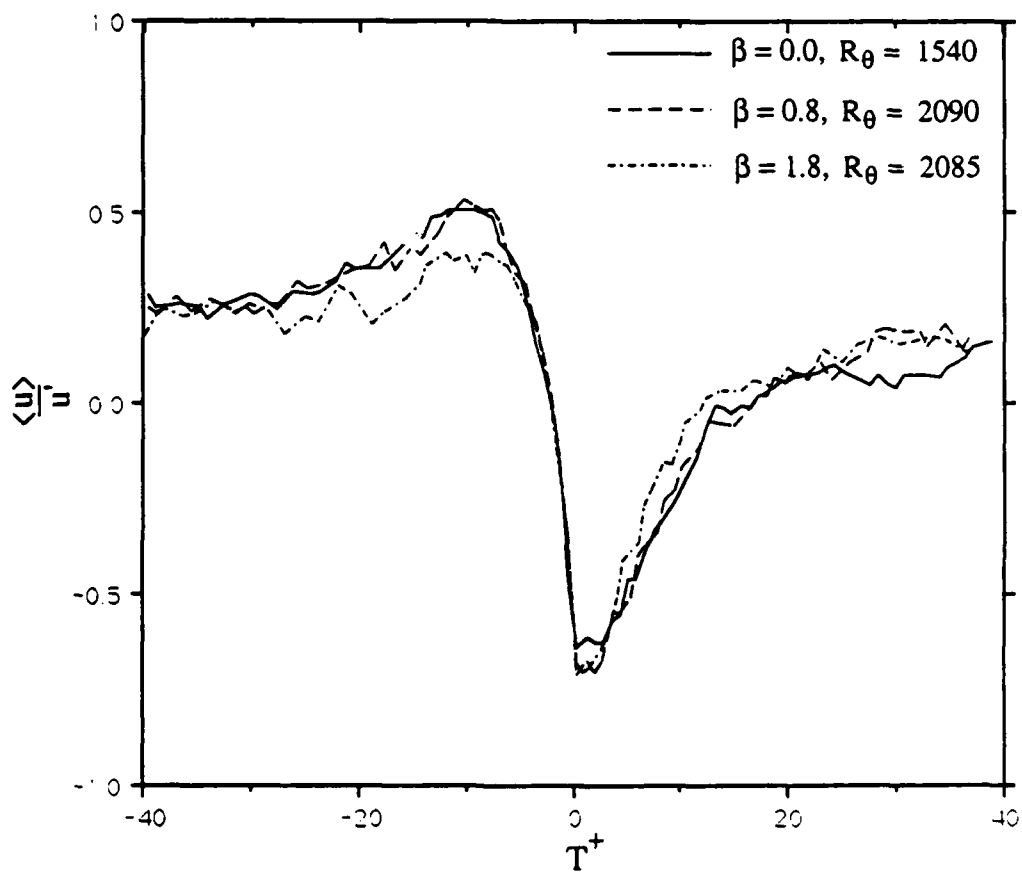


Figure 3.20. Conditionally averaged streamwise velocity signals centered on the burst leading edge.

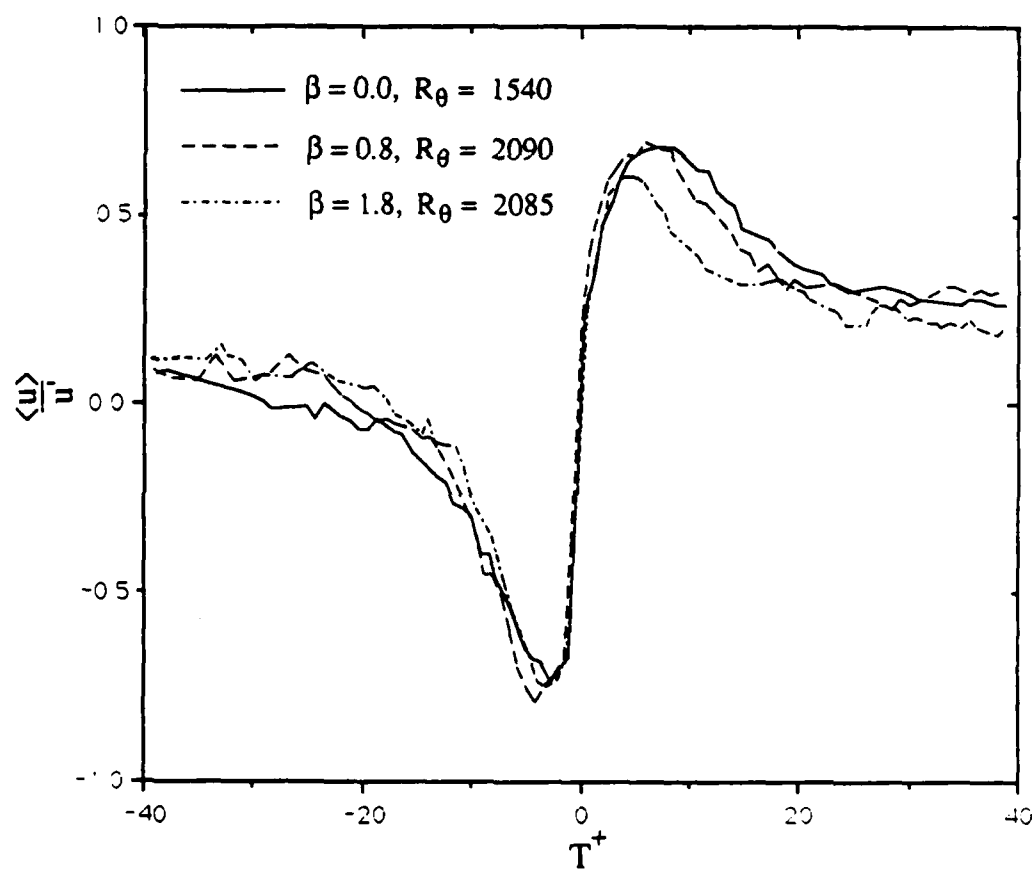


Figure 3.21. Conditionally averaged streamwise velocity signals centered on the burst trailing edge.

### 3.6.3 Number of Ejections per Burst

Tardu and Binder (1989) performed burst analysis of pulsatile flows. In the quasi-steady case he noted that the number of ejections occurring per burst varied with the pressure gradient. Tardu counted the number of ejections per burst using flow visualization techniques. Table 3.2 shows the number of ejections per burst at each experimental condition for the present study. Note that it is difficult to determine the precise number of ejections occurring per burst since the number of ejections varies with the threshold level,  $L$ . For purposes of this comparison, the maximum value of  $L$  which was still in the threshold independent region was used. These data indicate that the adverse pressure gradient tends to decrease the number of ejections per burst slightly. It appears however that this is not a large effect and does not indicate that the burst structure is greatly altered from that of the zero pressure gradient case.

Table 3.3 - Number of ejections per burst

$\beta$	$x$ (cm)	$Re$	$\frac{N_{eject}}{Burst}$	$L$
0.0	65.6	1260	3.2	0.6
0.0	90.1	1410	3.0	0.6
0.0	124.5	1540	2.7	0.7
0.8	66.5	1530	3.2	0.6
0.7	90.0	1780	2.6	0.6
0.8	125.0	2090	2.8	0.5
1.8	65.2	1796	2.5	0.5
1.8	90.0	2085	2.2	0.5
1.7	124.3	2495	2.3	0.5

## CHAPTER FOUR - CONCLUSIONS

This study has investigated the effect of Reynolds number and pressure gradient on the period of the burst cycle over a limited range of Reynolds number and pressure gradient parameter. It was shown that for each equilibrium boundary layer investigated, the burst period, normalized with inner variables, is not a function of the Reynolds number. The burst period,  $\bar{T}_b^+$ , was shown to be a function of the pressure gradient parameter alone with  $\bar{T}_b^+$  decreasing as the magnitude of the adverse pressure gradient parameter increases.

Studying the conditionally averaged burst signal indicates that while the pressure gradient affects the mean period of the bursting cycle, it does not seriously alter the mean velocity signature of the burst events taking place. Nevertheless, it appears that the number of ejections occurring per burst decreases slightly with increasing adverse pressure gradient.

The study indicated that the peak in the RMS of streamwise velocity moved physically outward from the wall with increased pressure gradient. When normalized with inner variables the peak remained at  $y^+ \approx 14-15$ . However, the value of the peak of the normalized RMS of streamwise velocity,  $u'^+$ , increased from  $u'^+ = 2.64$  for the zero pressure gradient case to  $u'^+ = 2.90$  for the strong adverse pressure gradient case.

This study gives an indication of how the burst period varies as a function Reynolds number and pressure gradient parameter. It appears that, for equilibrium or near-equilibrium flows, the Clauser (1954) equilibrium parameter,  $\beta$ , or the Clauser shape factor,  $G$ , are the proper parameters for characterizing the pressure gradient. Obviously, because of the limited range of Reynolds numbers and pressure gradients studied, further

work is needed to extend these findings to a wider range of applicability. Nevertheless, this data provides insight into how the influence of pressure gradient alters the burst structure and it will hopefully provide a useful database for developing improved turbulence models which include the important physics of the burst phenomena.

**LIST OF REFERENCES**

## LIST OF REFERENCES

- Bogard, D.G. and W.G. Tiederman 1986 Burst detection with single-point velocity measurements. *J. Fluid Mech.* 162, 389.
- Cebeci, T. and P. Bradshaw 1977 Momentum Transfer in Boundary Layers. Hemisphere Publishing Corp., pp 245-271.
- Clauser, F.H. 1954 Turbulent Boundary Layers in Adverse Pressure Gradients. *J. Aeronautical Sciences.* 24, pp 91-108
- Coles, D.E. and E.A. Hirst 1968 *Proc. Computation of Turbulent Boundary Layers.*, vol II, Dept. Mech. Eng., Stanford Univ., Stanford, CA., pp 1-54
- Corino, E.R. and R.S. Brodkey 1969 A visual investigation of the wall region in turbulent flow. *J. Fluid Mech.* 37, 1.
- Erm, L.P., A.J. Smits and P.N Joubert 1985 Low Reynolds number turbulent boundary layers on a smooth flat surface in a zero pressure gradient. *Proc. 5th Symp. on Turbulent Shear Flows, Ithaca, NY, August 7-9, 1985.*, pp 2.14-2.17
- Finnicum, D.S. and T.J. Hanratty 1988 Effect of Favorable Pressure Gradients on Turbulent Boundary Layers. *AIChE J.* 34, 529
- Harder, K.J. 1989 *Influence of wall strain rate, polymer concentration and channel upon drag reduction and turbulent structure.* MSME Thesis, Purdue University.
- Kim H.T., S.J. Kline and W.C. Reynolds 1971 The production of turbulence near a smooth wall in a turbulent boundary layer. *J. Fluid Mech.* 50, 133.
- Kline, S.J. Quasi-Coherent structures in the turbulent boundary layer. *Zoran P. Zaric' Memorial International Seminar on near wall turbulence, Dubrovnik, Yugoslavia, 16 - 20 May 1988.*
- Kline, S.J., W.C. Reynolds, F.A. Schraub and P.W. Rundstadler 1967 The Structure of Turbulent Boundary Layers. *J. Fluid Mech.* 30, 174
- Koskie, J.E., 1989 A note on corner stall avoidance by corner flow suction. Personal communication.
- Luchik, T.S. and W.G. Tiederman 1987 Timescale and structure of ejections and bursts in turbulent channel flows. *J. Fluid Mech.* 174, 529

- Luchik, T.S. and W.G. Tiederman 1988 Turbulent structure in low concentration drag-reducing flows. *J. Fluid Mech.* **190**, 241.
- Murlis, J., H.M. Tsai and P. Bradshaw 1982 The structure of turbulent boundary layers at low Reynolds numbers. *J. Fluid Mech.* **122**, 13.
- Purtell, L.P., P.S. Klebanoff and F.T. Buckley 1981 Characteristics of Turbulence in a Boundary Layer with Zero Pressure Gradient. *Phys. Fluids.* **24**, 123.
- Reneau, L.R., J.P. Johnston and S.J. Kline 1967 Performance and design of straight, two-dimensional diffusers. *J. Basic Engineering.* **43**, 141.
- Shah, D.A. and R.A. Antonia 1988 Scaling of the "bursting" period in turbulent boundary layer and duct flows. *Phys. Fluids.* **119**, 318.
- Simpson, R.L., J.H. Strickland and P.W. Barr 1977 Features of a separating turbulent boundary layer in the vicinity of separation. *J. Fluid Mech.* **79**, 553.
- Spalart, P. 1988 Direct simulation of a turbulent boundary layer up to  $Re_\theta = 1410$ . *J. Fluid Mech.* **187**, 61.
- Tardu, S. and G. Binder 1989 Ejections and bursts in pulsatile turbulent wall flow measurements and visualizations. *7th Symp. on Turbulent Shear Flows, Stanford University*, August 21-23, 1989.
- Walker, D.T. 1988 *Turbulent structure and mass transport in a channel flow with polymer injection*. Ph.D Thesis, Purdue University.
- Wei, T. and W.W. Willmarth 1989 Reynolds-number effects on the structure of a turbulent channel flow. *J. Fluid Mech.* **204**, 57.
- White, F.M. 1974 *Viscous Fluid Flow.*, McGraw-Hill, pp. 512-530.

**APPENDICES**

### A.1 Two-dimensionality verification

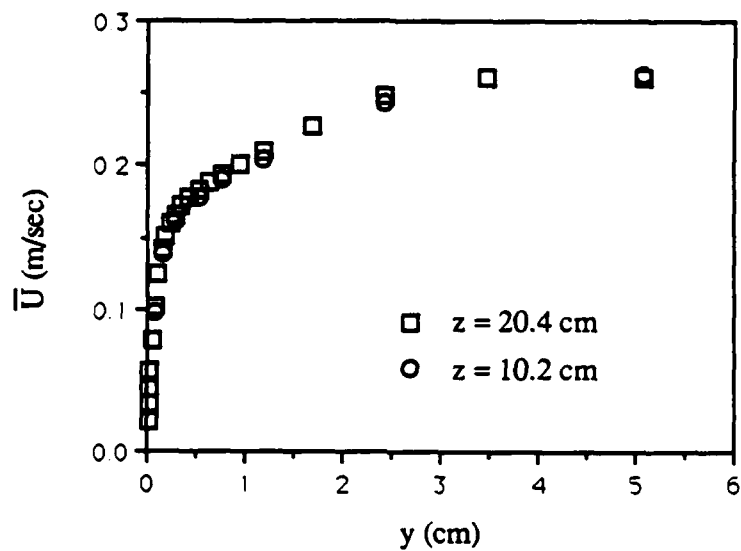


Figure A.1 Two-dimensionality verification for zero pressure gradient at station one.

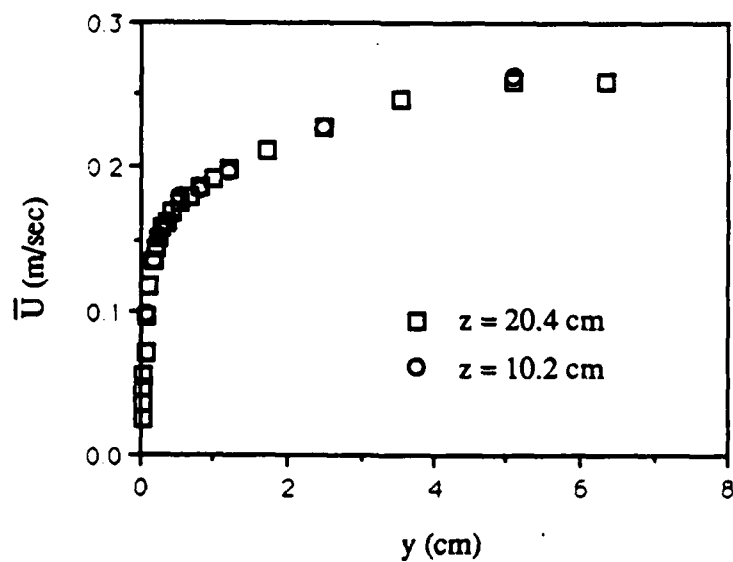


Figure A.2 Two-dimensionality verification for zero pressure gradient at station four.

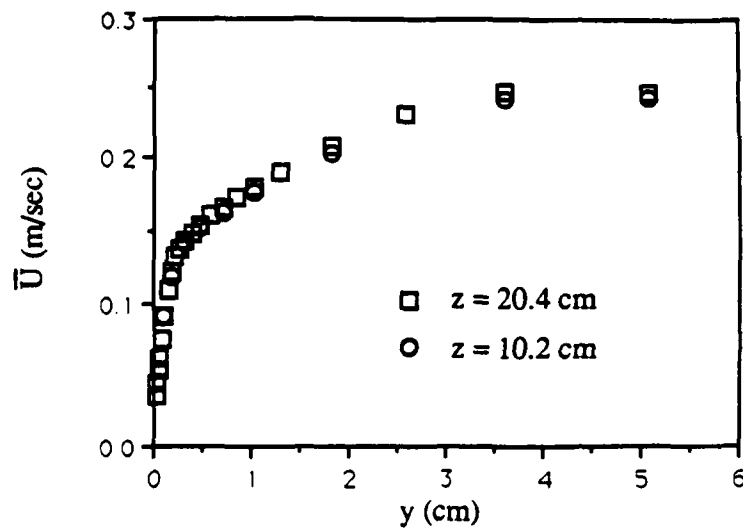


Figure A.3 Two-dimensionality verification for mild adverse pressure gradient at station one.

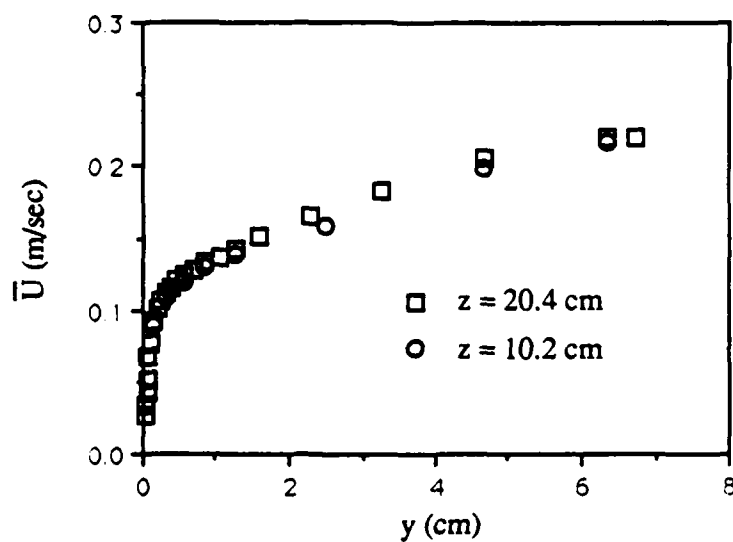


Figure A.4 Two-dimensionality verification for mild adverse pressure gradient at station four.

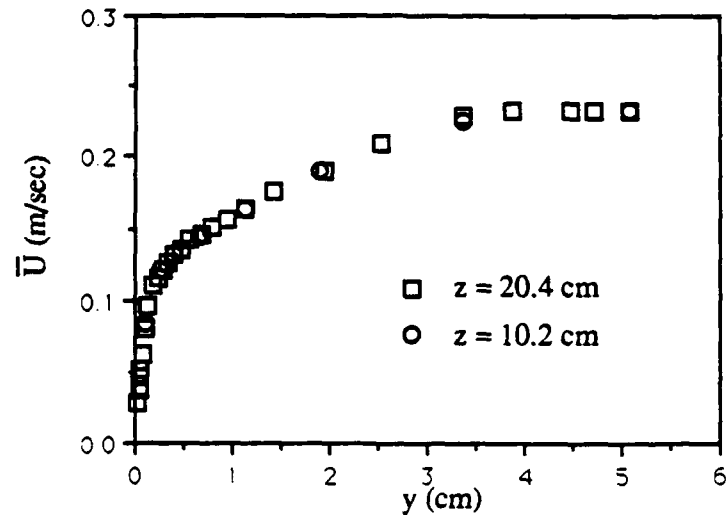


Figure A.5 Two-dimensionality verification for strong adverse pressure gradient at station one.

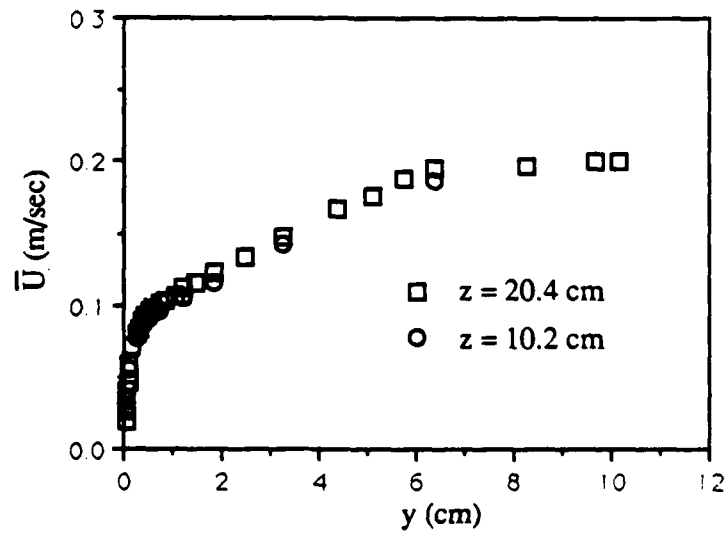


Figure A.6 Two-dimensionality verification for strong adverse pressure gradient at station four.

## Appendix B Uncertainty analysis

Determine uncertainty in  $u_\tau$ , where  $u_\tau$  is defined as

$$u_\tau = \left( v \frac{\bar{U}_1 - \bar{U}_2}{y_1 - y_2} \right)^{1/2}$$

The uncertainty in  $u_\tau$ ,  $u_{u_\tau}$ , is defined as

$$u_{u_\tau} = \pm \left[ \left( \frac{\bar{U}_1}{u_\tau} \frac{\partial u_\tau}{\partial U_1} u_{\bar{U}_1} \right)^2 + \left( \frac{\bar{U}_2}{u_\tau} \frac{\partial u_\tau}{\partial U_2} u_{\bar{U}_2} \right)^2 + \left( \frac{y_1}{u_\tau} \frac{\partial u_\tau}{\partial y_1} u_{y_1} \right)^2 + \left( \frac{y_2}{u_\tau} \frac{\partial u_\tau}{\partial y_2} u_{y_2} \right)^2 \right]^{1/2} \quad (\text{A.1})$$

derivatives of  $u_\tau$

$$\frac{\partial u_\tau}{\partial U_1} = \frac{1}{2} v^{1/2} (\bar{U}_1 - \bar{U}_2)^{-1/2} (y_1 - y_2)^{-1/2} (1) \quad (\text{A.2})$$

$$\frac{\partial u_\tau}{\partial U_2} = \frac{1}{2} v^{1/2} (\bar{U}_1 - \bar{U}_2)^{-1/2} (y_1 - y_2)^{-1/2} (-1) \quad (\text{A.3})$$

$$\frac{\partial u_\tau}{\partial y_1} = -\frac{1}{2} v^{1/2} (\bar{U}_1 - \bar{U}_2)^{-1/2} (y_1 - y_2)^{-3/2} (1) \quad (\text{A.4})$$

$$\frac{\partial u_\tau}{\partial y_2} = -\frac{1}{2} v^{1/2} (\bar{U}_1 - \bar{U}_2)^{-1/2} (y_1 - y_2)^{-3/2} (-1) \quad (\text{A.5})$$

applying equations A.2 - A.5 to equation A.1 yields

$$u_{u_\tau} = \pm \left[ \left( \frac{1}{2} \frac{\bar{U}_1}{U_1 - U_2} u_{\bar{U}_1} \right)^2 + \left( \frac{1}{2} \frac{\bar{U}_2}{U_1 - U_2} u_{\bar{U}_2} \right)^2 + \left( \frac{1}{2} \frac{-y_1}{y_1 - y_2} u_{y_1} \right)^2 + \left( \frac{1}{2} \frac{y_2}{y_1 - y_2} u_{y_2} \right)^2 \right]^{1/2} \quad (\text{A.6})$$

Typical values of  $\bar{U}_1$ ,  $\bar{U}_2$ ,  $y_1$  and  $y_2$  are

$$y_1 = 0.406 \text{ mm} \qquad \bar{U}_1 = 0.0555 \text{ m/sec}$$

$$y_2 = 0.254 \text{ mm} \qquad \bar{U}_2 = 0.0346 \text{ m/sec}$$

$y$  can be measured to within  $\pm 0.00635$  cm. Thus,

$$u_{y_1} = \frac{0.00635}{0.406} = 0.0156$$

$$u_{y_2} = \frac{0.00635}{0.254} = 0.0250$$

Based on the 5000 data points collected the uncertainty in the average velocity is

$$u_{\bar{U}_1} = u_{\bar{U}_2} = 0.015$$

Using the typical values and uncertainties given above in equation A.6

$$u_{u_\tau} = 0.038$$

Thus

$$u_{u_\tau} = 3.8\% \text{ with 95\% confidence}$$

**Appendix C - Wall Shapes**

Table C.1 Wall shape for zero pressure gradient case

<u>x(cm)</u>	<u>y(cm)</u>
0.0	20.32
116.8	20.96
132.1	21.04
147.3	21.10
162.6	21.17
177.8	21.23
193.0	21.30
208.3	21.37
223.5	21.44
238.8	21.50
254.0	21.56

Table C.2 Wall shape for mild adverse pressure gradient case

<u>x(cm)</u>	<u>y(cm)</u>
0.0	20.6
116.8	21.0
132.1	21.4
147.3	23.3
162.6	24.2
177.8	24.8
193.0	25.5
208.3	26.1
223.5	26.7
238.8	27.5
254.0	28.2

Table C.3 Wall shape for strong adverse pressure gradient case

<u>x(cm)</u>	<u>y(cm)</u>
0.0	20.6
116.8	21.6
132.1	22.7
147.3	24.8
162.6	26.0
177.8	27.5
193.0	28.7
208.3	29.8
223.5	30.6
238.8	31.44
254.0	32.18

## Appendix D - Tabulated Velocity Data

Table D.1 - Zero pressure gradient - station 1

$R_\theta = 1120$   $u_\tau = 12.0 \text{ mm/sec}$   $\delta^* = 0.57 \text{ cm}$   $\theta = 0.39 \text{ cm}$   $H = 1.47$

y(mm)	$y^+$	U (m/sec)	$U^+$	$u'$ (m/sec)	$u'^+$
50.800	669.890	0.261	21.775	0.00189	0.158
34.620	456.530	0.261	21.750	0.00319	0.266
24.181	318.868	0.249	20.717	0.0124	1.033
16.891	222.738	0.227	18.917	0.0175	1.458
11.811	155.749	0.209	17.433	0.0190	1.622
9.449	124.600	0.201	16.750	0.0195	1.622
7.747	102.158	0.194	16.167	0.0208	1.733
6.350	83.736	0.189	15.750	0.0208	1.733
5.207	68.664	0.182	15.208	0.0216	1.797
4.267	56.271	0.177	14.750	0.0230	1.916
3.480	45.887	0.172	14.333	0.0238	1.983
2.870	37.849	0.165	13.750	0.0251	2.092
2.337	30.815	0.159	13.250	0.0276	2.300
1.930	25.456	0.151	12.583	0.0295	2.458
1.575	20.767	0.142	11.858	0.0305	2.542
1.118	14.738	0.124	10.333	0.0311	2.592
0.787	10.383	0.102	8.500	0.0301	2.508
0.539	7.369	0.079	6.583	0.0267	2.225
0.381	5.024	0.057	4.750	0.0213	1.775
0.305	4.019	0.045	3.750	0.0168	1.400
0.229	3.015	0.034	2.833	0.0133	1.109
0.152	2.010	0.022	1.833	0.00886	0.738

Table D.2 - Zero pressure gradient - station 2

$R_\theta = 1257$     $u_\tau = 11.8$  mm/sec    $\delta^* = 0.64$  cm    $\theta = 0.44$  cm    $H = 1.47$

y(mm)	$y^+$	U (m/sec)	$U^+$	$u'$ (m/sec)	$u'^+$
50.724	657.737	0.261	22.119	0.00216	0.183
41.326	535.874	0.261	22.119	0.00292	0.247
31.953	414.339	0.256	21.695	0.00858	0.727
22.682	294.121	0.237	20.085	0.0153	1.297
16.078	208.487	0.219	18.559	0.0178	1.508
11.405	147.884	0.205	17.373	0.0194	1.644
9.093	117.912	0.196	16.610	0.0205	1.737
7.442	96.503	0.190	16.102	0.0206	1.746
6.096	79.047	0.184	15.593	0.0216	1.831
4.978	64.555	0.178	15.085	0.0225	1.907
4.064	52.698	0.174	14.746	0.0234	1.983
3.327	43.147	0.169	14.322	0.0245	2.076
2.692	34.912	0.162	13.729	0.0264	2.237
2.210	28.655	0.155	13.136	0.0280	2.373
1.778	23.055	0.146	12.373	0.0301	2.551
1.448	18.788	0.135	11.441	0.0312	2.644
1.016	13.175	0.117	9.915	0.0312	2.644
0.686	8.893	0.093	7.881	0.0291	2.466
0.457	5.929	0.067	5.678	0.0236	2.000
0.305	3.952	0.046	3.924	0.0176	1.506
0.229	2.964	0.036	3.051	0.0135	1.144
0.152	1.978	0.024	2.034	0.00940	0.797

Table D.3 - Zero pressure gradient - station 3

$R_\theta = 1410$     $u_\tau = 11.7$  mm/sec    $\delta^* = 0.71$  cm    $\theta = 0.49$  cm    $H = 1.44$

y(mm)	$y^+$	U (m/sec)	$U^+$	$u'$ (m/sec)	$u'^+$
50.800	653.142	0.262	22.393	0.00232	0.198
41.910	538.842	0.260	22.222	0.00388	0.332
33.934	436.299	0.253	21.624	0.00937	0.801
23.698	304.691	0.233	19.915	0.0157	1.342
16.561	212.924	0.216	18.462	0.0178	1.521
11.481	147.610	0.201	17.179	0.0194	1.658
9.246	118.872	0.194	16.581	0.0198	1.692
7.595	97.645	0.188	16.068	0.0207	1.769
6.223	80.010	0.182	15.556	0.0215	1.838
5.105	65.641	0.176	15.043	0.0222	1.897
4.166	53.558	0.171	14.615	0.0229	1.957
3.429	44.087	0.166	14.188	0.0241	2.060
2.794	35.923	0.161	13.761	0.0262	2.239
2.286	29.391	0.153	13.077	0.0278	2.376
1.880	24.166	0.147	12.564	0.0292	2.496
1.549	19.921	0.135	11.538	0.0304	2.598
1.092	14.043	0.117	10.000	0.0312	2.667
0.762	9.797	0.096	8.205	0.0291	2.487
0.533	6.858	0.074	6.325	0.0247	2.109
0.381	4.899	0.056	4.769	0.0207	1.769
0.305	3.919	0.044	3.761	0.0168	1.436
0.229	2.939	0.034	2.906	0.0130	1.111
0.152	1.959	0.023	1.966	0.00930	0.795

Table D.4 - Zero pressure gradient - station 4

$R_\theta = 1540$     $u_\tau = 11.4 \text{ mm/sec}$     $\delta^* = 0.77 \text{ cm}$     $\theta = 0.54 \text{ cm}$     $H = 1.43$

$y(\text{mm})$	$y^+$	$U \text{ (m/sec)}$	$U^+$	$u' \text{ (m/sec)}$	$u'^+$
50.724	657.737	0.261	22.119	0.00216	0.183
63.500	795.495	0.259	22.719	0.00200	0.175
50.800	636.396	0.260	22.807	0.00314	0.275
35.484	444.523	0.246	21.579	0.0119	1.046
24.867	310.561	0.228	20.000	0.0158	1.388
17.323	217.011	0.212	18.596	0.0175	1.535
12.090	151.462	0.198	17.368	0.0190	1.671
9.677	121.233	0.192	16.842	0.0198	1.734
7.925	99.278	0.186	16.316	0.0200	1.754
6.502	81.459	0.180	15.789	0.0210	1.839
5.334	66.822	0.175	15.351	0.0219	1.925
4.369	54.730	0.168	14.737	0.0233	2.045
3.581	44.866	0.162	14.211	0.0242	2.121
2.921	36.593	0.158	13.860	0.0251	2.201
2.413	30.229	0.151	13.281	0.0265	2.324
1.981	24.819	0.144	12.632	0.0285	2.499
1.626	20.365	0.135	11.842	0.0299	2.621
1.143	14.319	0.117	10.263	0.0305	2.671
0.813	10.182	0.096	8.404	0.0296	2.593
0.559	7.000	0.071	6.268	0.0243	2.131
0.406	5.091	0.055	4.864	0.0210	1.838
0.330	4.137	0.046	4.026	0.0180	1.575
0.254	3.182	0.036	3.167	0.0139	1.220
0.178	2.227	0.024	2.132	0.00978	0.858

Table D.5 - Mild adverse pressure gradient - station 1

$R_\theta = 1265$   $u_\tau = 10.4$  mm/sec  $\delta^* = 0.72$  cm  $\theta = 0.47$  cm  $H = 1.54$

y(mm)	$y^+$	U (m/sec)	$U^+$	$u'$ (m/sec)	$u'^+$
50.800	580.571	0.247	23.731	0.00220	0.212
36.119	412.786	0.246	23.702	0.00390	0.375
25.832	295.221	0.230	22.144	0.0140	1.346
18.288	209.006	0.207	19.933	0.194	1.865
13.005	148.626	0.189	18.212	0.0203	1.952
10.389	118.727	0.179	17.202	0.0209	2.010
8.534	97.536	0.172	16.529	0.0211	2.029
6.985	79.929	0.164	15.817	0.0215	2.067
5.715	65.314	0.159	15.279	0.0221	2.125
4.699	53.703	0.154	14.760	0.0227	2.183
2.835	43.833	0.147	14.144	0.0240	2.308
3.150	35.995	0.142	13.635	0.0248	2.385
2.591	29.609	0.136	13.087	0.0263	2.529
2.108	24.094	0.131	12.577	0.0279	2.683
1.727	19.739	0.121	11.654	0.0284	2.731
1.448	16.546	0.109	10.462	0.0294	2.827
0.940	10.741	0.090	8.644	0.0283	2.721
0.711	8.128	0.074	7.154	0.0262	2.519
0.508	5.806	0.063	6.058	0.0237	2.279
0.432	4.935	0.054	5.173	0.0211	2.029
0.356	4.064	0.045	4.317	0.0184	1.769
0.279	3.193	0.036	3.423	0.0150	1.442

Table D.6 - Mild adverse pressure gradient - station 2

$R_\theta = 1530$ $u_\tau = 9.4 \text{ mm/sec}$ $\delta^* = 0.92 \text{ cm}$ $\theta = 0.59 \text{ cm}$ $H = 1.55$					
$y(\text{mm})$	$y^+$	$U \text{ (m/sec)}$	$U^+$	$u' \text{ (m/sec)}$	$u'^+$
57.150	590.341	0.234	24.883	0.00220	0.245
50.800	824.747	0.234	24.947	0.00230	0.362
41.707	430.817	0.233	24.777	0.00340	0.638
36.754	379.655	0.227	24.181	0.00600	1.085
29.134	300.943	0.211	22.447	0.0152	1.617
20.345	210.161	0.188	19.989	0.0187	1.989
14.224	146.929	0.170	18.043	0.0191	2.032
11.379	117.543	0.162	17.266	0.0201	2.138
9.322	96.291	0.154	16.426	0.0207	2.202
7.645	78.974	0.149	15.872	0.0203	2.160
6.248	64.544	0.142	15.160	0.0204	2.170
5.131	52.999	0.138	14.660	0.0210	2.234
4.216	43.554	0.134	14.298	0.0216	2.298
3.454	35.683	0.130	13.872	0.0227	2.415
2.819	29.123	0.123	13.106	0.0235	2.500
2.311	23.876	0.117	12.500	0.0244	2.596
1.905	19.678	0.110	11.691	0.0253	2.691
1.397	14.431	0.100	10.681	0.0267	2.840
1.041	10.757	0.086	9.128	0.256	2.723
0.762	7.871	0.070	7.468	0.0241	2.564
0.559	5.772	0.056	5.979	0.0208	2.213
0.457	4.723	0.047	5.043	0.0182	1.936
0.381	3.936	0.040	4.213	0.0159	1.691
0.279	2.886	0.029	3.096	0.0123	1.309

Table D.7 - Mild adverse pressure gradient - station 3

$R_\theta = 1780$	$u_\tau = 9.1 \text{ mm/sec}$	$\delta^* = 1.08 \text{ cm}$	$\theta = 0.70 \text{ cm}$	$H = 1.56$	
$y(\text{mm})$	$y^+$	$U \text{ (m/sec)}$	$U^+$	$u' \text{ (m/sec)}$	$u'^+$
67.310	673.100	0.229	25.143	0.00206	0.226
63.500	635.000	0.228	25.110	0.00229	0.252
57.150	571.500	0.229	25.165	0.00280	0.308
50.800	508.000	0.227	24.923	0.00510	0.560
49.993	439.928	0.222	24.396	0.00930	1.022
30.734	307.340	0.199	21.824	0.0162	1.780
21.463	214.630	0.177	19.462	0.0186	2.044
15.011	150.114	0.163	17.901	0.0191	2.099
11.989	119.888	0.154	16.967	0.0192	2.110
9.830	98.298	0.148	16.220	0.0196	2.154
8.052	80.518	0.143	15.703	0.0195	2.143
6.604	66.040	0.139	15.319	0.0198	2.176
5.410	54.102	0.135	14.835	0.0206	2.264
4.445	44.450	0.130	14.319	0.0208	2.286
3.632	36.322	0.124	13.626	0.0222	2.440
4.496	29.718	0.120	13.209	0.0228	2.505
2.438	24.384	0.113	12.462	0.0236	2.593
2.007	20.066	0.108	11.820	0.0243	2.670
1.473	14.732	0.097	10.659	0.0254	2.791
1.092	10.922	0.082	9.055	0.0249	2.736
0.813	8.128	0.069	7.626	0.0233	2.560
0.584	5.842	0.053	5.802	0.0198	2.176
0.463	4.826	0.044	4.824	0.0173	1.901
0.356	3.556	0.032	3.527	0.0133	1.462
0.279	2.794	0.025	2.747	0.0106	1.165

Table D.8 - Mild adverse pressure gradient - station 4

$R_\theta = 2090$     $u_\tau = 8.5$  mm/sec    $\delta^* = 1.32$  cm    $\theta = 0.86$  cm    $H = 1.54$

y(mm)	$y^+$	U (m/sec)	$U^+$	$u'$ (m/sec)	$u'^+$
67.310	636.116	0.220	25.640	0.00267	0.314
63.500	600.110	0.220	25.640	0.00267	0.314
46.538	440.001	0.206	23.919	0.0120	1.407
23.512	307.256	0.183	21.291	0.0162	1.907
22.708	214.599	0.165	19.209	0.0173	2.035
15.875	150.027	0.151	17.570	0.0188	2.221
12.700	120.022	0.143	16.581	0.0185	2.174
10.414	98.418	0.137	15.953	0.0186	2.186
8.534	80.655	0.132	15.395	0.0183	2.151
6.985	66.012	0.129	14.953	0.0192	2.256
5.715	54.010	0.125	14.547	0.0194	2.279
4.699	44.408	0.120	14.012	0.0202	2.372
3.835	36.247	0.116	13.500	0.0211	2.477
3.150	29.765	0.112	12.988	0.02187	2.570
2.591	24.484	0.107	12.465	0.0220	2.593
2.108	19.924	0.101	11.744	0.0228	2.686
1.575	14.883	0.093	10.767	0.0242	2.849
1.168	11.042	0.077	8.930	0.0238	2.802
0.864	8.161	0.067	7.779	0.0223	2.628
0.660	6.241	0.051	5.965	0.0191	2.244
0.559	5.281	0.043	5.000	0.0169	1.988
0.457	4.321	0.035	4.023	0.0138	1.628
0.356	3.361	0.027	3.093	0.0109	1.279

Table D.9 - Strong adverse pressure gradient - station 1

$R_\theta = 1315$     $u_\tau = 8.8 \text{ mm/sec}$     $\delta^* = 0.82 \text{ cm}$     $\theta = 0.52 \text{ cm}$     $H = 1.58$

$y(\text{mm})$	$y^+$	$U \text{ (m/sec)}$	$U^+$	$u' \text{ (m/sec)}$	$u'^+$
50.851	49.744	0.232	26.409	0.00240	0.273
47.411	45.900	0.232	26.364	0.00320	0.364
44.856	433.776	0.232	26.386	0.00370	0.420
38.659	373.843	0.232	26.386	0.00460	0.473
33.680	325.701	0.230	26.102	0.00820	0.932
25.298	244.644	0.209	23.739	0.0168	1.909
19.456	188.150	0.190	21.580	0.0195	2.216
14.275	138.042	0.175	19.886	0.0206	2.341
11.430	110.532	0.163	18.568	0.0208	2.364
9.530	92.356	0.157	17.795	0.0213	2.420
8.001	77.372	0.151	17.170	0.0212	2.409
6.731	65.091	0.146	16.636	0.0217	2.466
5.613	54.283	0.141	16.057	0.0222	2.523
4.699	45.441	0.136	15.409	0.0224	2.545
3.937	38.072	0.132	14.966	0.0235	2.670
3.302	31.931	0.126	14.284	0.0237	2.693
2.769	26.773	0.121	13.761	0.0251	2.852
2.311	22.352	0.116	13.205	0.0256	2.909
1.956	18.913	0.111	12.557	0.0260	2.955
1.397	13.509	0.096	10.920	0.0271	3.080
0.991	9.579	0.080	9.045	0.0262	2.977
0.737	7.123	0.062	7.102	0.0230	2.614
0.610	5.895	0.052	5.886	0.0209	2.375
0.533	5.158	0.045	5.159	0.0189	2.148
0.432	4.176	0.038	4.295	0.0166	1.886
0.330	3.193	0.028	3.193	0.0127	1.443

Table D.10 - Strong adverse pressure gradient - station 2

$R_\theta = 1796$   $u_\tau = 8.4 \text{ mm/sec}$   $\delta^* = 1.22 \text{ cm}$   $\theta = 0.75 \text{ cm}$   $H = 1.63$

y(mm)	$y^+$	U (m/sec)	$U^+$	$u'$ (m/sec)	$u'^+$
63.500	586.154	0.220	26.155	0.00290	0.345
57.150	527.538	0.220	26.190	0.00370	0.440
50.800	468.923	0.218	25.917	0.00440	0.524
44.450	410.308	0.215	25.548	0.00780	0.929
38.430	354.740	0.205	24.440	0.0136	1.619
28.854	266.348	0.181	21.607	0.0172	2.048
21.641	199.761	0.163	19.393	0.0193	2.298
16.256	150.055	0.148	17.679	0.0192	2.286
13.005	120.044	0.141	16.726	0.0199	2.369
10.871	100.350	0.134	15.929	0.0195	2.321
9.093	83.937	0.129	15.321	0.0198	2.357
7.595	70.104	0.124	14.726	0.0199	2.369
6.350	58.615	0.120	14.286	0.0195	2.321
5.334	49.237	0.115	13.750	0.0201	2.393
4.445	41.031	0.111	13.274	0.0209	2.488
3.708	34.231	0.109	12.917	0.0213	2.536
3.099	28.604	0.104	12.357	0.0225	2.649
2.591	23.915	0.100	11.845	0.0223	2.655
2.159	19.929	0.095	11.286	0.0227	2.702
1.524	14.068	0.083	9.857	0.0238	2.833
0.787	7.268	0.052	6.155	0.0201	2.393
0.635	5.862	0.048	5.714	0.198	2.298
0.533	4.924	0.040	4.798	0.0169	2.012
0.381	3.517	0.028	3.357	0.0125	1.488
0.279	2.579	0.020	2.321	0.0090	1.071

Table D.11 - Strong adverse pressure gradient - station 3

$R_\theta = 2085$   $u_\tau = 7.6$  mm/sec  $\delta^* = 1.48$  cm  $\theta = 0.90$  cm  $H = 1.64$

y(mm)	$y^+$	U (m/sec)	$U^+$	$u'$ (m/sec)	$u'^+$
66.04	551.543	0.210	27.658	0.00340	0.447
63.500	530.330	0.210	27.618	0.00410	0.539
57.150	477.297	0.207	27.303	0.00520	0.684
50.800	424.264	0.203	26.645	0.00880	1.158
45.720	381.837	0.194	25.487	0.0130	1.711
41.377	345.563	0.187	24.553	0.0151	1.987
31.064	259.437	0.167	21.921	0.0177	2.329
23.317	194.737	0.149	19.605	0.0189	2.487
17.500	146.159	0.137	17.987	0.0189	2.487
13.995	116.885	0.126	16.632	0.0191	2.513
11.709	97.793	0.122	15.987	0.0187	2.461
9.779	81.671	0.117	15.408	0.0185	2.434
8.179	68.306	0.115	15.105	0.0188	2.474
6.833	57.063	0.111	14.553	0.0192	2.526
5.715	47.730	0.107	14.092	0.0190	2.500
4.775	39.881	0.103	13.605	1.0189	2.487
3.988	33.305	0.100	13.224	0.0197	2.592
3.327	27.789	0.096	12.618	0.0202	2.658
2.794	23.335	0.092	12.132	0.0212	2.789
2.337	19.516	0.088	11.553	0.0214	2.816
1.651	13.789	0.076	0.053	0.0220	2.895
1.168	9.758	0.065	8.605	0.0214	2.816
0.813	6.788	0.052	6.908	0.0199	2.618
0.686	5.728	0.044	5.789	0.0178	2.342
0.584	4.879	0.039	5.158	0.0165	2.171
0.457	3.818	0.031	4.092	0.0134	1.763
0.356	2.970	0.025	3.263	0.0113	1.487

Table D.12 - Strong adverse pressure gradient - station 4

$R_\theta = 2495$   $u_\tau = 7.0$  mm/sec  $\delta^* = 1.86$  cm  $\theta = 1.13$  cm  $H = 1.64$

y(mm)	$y^+$	U (m/sec)	$U^+$	$u'$ (m/sec)	$u'^+$
101.600	781.540	0.200	28.629		
96.770	744.417	0.201	28.729		
82.550	635.001	0.197	28.200		
63.500	488.462	0.196	27.957	0.0084	1.200
57.150	439.616	0.188	26.814	0.0121	1.729
50.800	390.770	0.176	25.114	0.0146	2.086
43.612	335.476	0.167	23.786	0.0156	2.229
32.741	35.851	0.147	21.071	0.0177	2.529
24.587	189.133	0.133	18.929	0.0183	2.614
18.440	141.850	0.122	17.500	0.0176	2.514
14.757	113.519	0.115	16.471	0.0173	2.471
12.344	94.957	0.112	16.057	0.0172	2.457
10.312	79.326	0.107	15.271	0.0164	2.343
8.611	66.236	0.103	14.743	0.0175	2.500
7.214	55.789	0.101	14.443	0.0174	2.486
6.020	46.306	0.097	13.886	0.0177	2.529
5.029	38.686	0.095	13.614	0.0172	2.457
4.216	32.434	0.092	13.143	0.0189	2.700
3.531	27.159	0.088	13.586	0.0192	2.743
2.946	22.665	0.083	11.871	0.0193	2.757
2.388	18.366	0.079	11.357	0.0193	2.575
1.727	13.286	0.071	10.171	0.0205	2.929
1.219	9.378	0.059	8.357	0.0194	2.771
0.864	6.643	0.047	6.686	0.0176	2.514
0.737	5.666	0.041	5.857	0.0163	2.329
0.610	4.689	0.035	4.929	0.0142	2.029
0.483	3.712	0.027	3.900	0.0116	1.657
0.356	2.735	0.020	2.900	0.00900	1.286

## DISTRIBUTION LIST

Dr. Michael M. Reischman, Code 1132F  
Office of Naval Research  
800 North Quincy Street  
Arlington, VA 22217-5000

Office of Naval Research  
Resident Representative  
536 Clark Street, Rm. 286  
Chicago, IL 60605-1588

Greg Anderson  
Code 634  
Naval Ocean System Center  
San Diego, CA 92152

Prof. R.F. Blackwelder  
University of Southern California  
Dept. of Aerospace Engineering  
University Park  
Los Angeles, CA 90089-1191

Prof. D.G. Bogard  
Department of Mechanical Engineering  
The University of Texas  
Austin, TX 78712

Dr. Steve Deutsche  
ARL  
Pennsylvania State University  
P.O. Box 30  
State College, PA 16801

Prof. T.J. Hanratty  
Dept. of Chemical Engineering  
1209 West California Street  
Box C-3  
Urbana, IL 61801

Defense Technical Information Center  
Building 5, Cameron Station  
Alexandria, VA 22314  
(12 copies)

Mechanical Engineering Business Office  
Purdue University  
West Lafayette, IN 47907

Dr. R.J. Hansen  
Code 1215  
Office of Naval Research  
800 North Quincy Street  
Arlington, VA 22217

Dr. J.H. Haritonidis  
Room 37-461  
Massachusetts Institute of Technology  
Cambridge, MA 02139

Eric W. Hendricks  
Code 634  
Naval Ocean System Center  
San Diego, CA 92152

Mr. G.W. Jones  
DARPA/NTO  
1515 Wilson Blvd.  
Arlington, VA 22209

Dr. John Kim  
M.S. 202A-1  
NASA - Ames Research Center  
Moffett Field, CA 94035

Dr. O. Kim  
Code 6124  
Naval Research Laboratory  
Washington, DC 20375

J.D. Swearingen  
Code 4420  
Naval Research Laboratory  
Washington, DC 20375

Prof. S.J. Kline  
Thermosciences Division  
Dept. of Mechanical Engineering  
Stanford University  
Stanford, CA 94305

Prof. David T. Walker  
Dept. of Naval Architecture  
and Marine Engineering  
North Campus  
Ann Arbor, MI 48109-2145

G. Leal  
Dept. of Chemical & Nuclear Engineering  
University of California  
Santa Barbara, CA 93106

Prof. W.W. Willmarth  
Dept. of Aerospace Engineering  
University of Michigan  
Ann Arbor, MI 48109

Justin H. McCarthy  
Code 1540  
David Taylor Research Center  
Bethesda, MD 20084

Dr. C.L. Merkle  
Dept. of Mechanical Engineering  
Pennsylvania State University  
State College, PA 16801

Richard H. Nadolink  
Code 821  
Naval Underwater Systems Center  
Bldg. 679/1  
Newport, RI 02841-5047

Steve Robinson  
M.S. 229-1  
NASA - Ames Research Center  
Moffett Field, CA 94035

W.G. Souders  
Code 1543  
David Taylor Research Center  
Bethesda, MD 20084